Universal Time Variations in the Magnetosphere and the Effect of CME Arrival Time: Analysis of the February 2022 Event that Led to the Loss of Starlink Satellites

M. Lockwood[1], M.J. Owens[1], and L.A. Barnard[1]

[1]Department of Meteorology, University of Reading, Reading, Berkshire, RG6 6BB, UK

Key Points:

- Analysis of the CME effects causing the loss of 38 Starlink satellites shows that the terrestrial response to a CME depends on its impact UT
- UT effects are caused by diurnal motions of the poles and the eccentric nature of the geomagnetic field
- Joule heating dominated in the southern polar cap during the first CME and initially during the second but later was dominant in the north

Corresponding author: Mike Lockwood, `m.lockwood@reading.ac.uk`

Abstract

We present an analysis of the magnetospheric response to the two Coronal Mass Ejection (CME) impacts which led to the destruction of 38 out of 49 Starlink satellites in early February 2022. We employ the Expanding-Contracting Polar Cap model to analyse the variation in the size of the ionospheric polar caps and thereby quantify the Universal Time (UT) effect of the diurnal motions of the geomagnetic poles in a geocentric frame of reference. The results show that use of quasi-steady convection model predicts a very similar global power deposition into the thermosphere as that inferred here, but does not give the same division of that power between the northern and southern hemispheres. We demonstrate that, through the combined effects of the Russell-McPherron dipole-tilt mechanism on solar-wind magnetosphere coupling and of the diurnal polar cap motions in a geocentric frame, the power deposited varies significantly with the arrival UT of the CMEs at Earth. We show that in the events of early February 2022, both CMEs arrived at almost the optimum UT to cause maximum thermospheric heating.

Plain Language Summary

In early February 2022, 38 out of 49 Starlink satellites burned up in Earth's atmosphere because two Coronal Mass Ejections emitted from the Sun hit the Earth and had a larger heating effect on the upper atmosphere than expected. Using recent understanding of how Earth's magnetic field responds to such impacts, we show that the heating in the southern polar cap dominated after the first impact and initially during the second impact but then moved to the northern hemisphere. We show that the effect would have been less severe had the CMEs arrived either earlier or later than they did.

1 Introduction

1.1 The events of 3-4 February, 2022

The impact of two Coronal Mass Ejections (CMEs) on Earth's magnetosphere on 3 and 4 February 2022 caused the loss of 38 of 49 recently-launched SpaceX Starlink satellites due to enhanced upper atmosphere density during the resulting geomagnetic storm. (Hapgood et al., 2022; Fang et al., 2022; Kataoka et al., 2022; Tsurutani et al., 2022; Y. Zhang et al., 2022; Dang et al., 2022). The full financial cost of this space weather event is not known but has been estimated to be upward of $20m for the lost satellites and $30m for the wasted launch capacity. A surprising element of this event is that the causal geomagnetic disturbance was moderately large but not extreme. The global geomagnetic activity Kp index reached a value of 5+ after the impact of each CME, a value exceeded 3.5% of the time since production of the Kp index began in 1932 (Bartels et al., 1939; Bartels, 1949). This level meant that the event was classified as a minor storm according to the scale used by NOAA's Space Weather Prediction Centre (SWPC). The 3-hourly global am geomagnetic index (Mayaud, 1972) indicates a slightly rarer event, reaching 84nT after both CMEs - a level that is exceeded 2% of the time since the am index data series began in January 1959.

On 3 February 2022, at 18:13 UTC, the Starlink satellites had been launched by a SpaceX Falcon 9 rocket from NASA's Kennedy Space Center in Florida into an orbit with perigee of 210 km. This was the 36th in a series of such launches since May 2019. However the geomagnetic storm, which at the time of launch had just begun, subsequently raised the density of the atmosphere, increasing the drag on the satellites and induced re-entry before the planned deployment of electric thrusters could raise all but 11 of them to an operational orbit at altitude near 500 km. Consequently, 38 of the 49 satellites burnt up in the atmosphere on 7 February. SpaceX has responded to the loss by changing its launch procedures: the subsequent Starlink launch on 21 February used a higher initial orbit at 300 km altitude, but carried only 46 instead of 49 satellites. It should be noted

that SpaceX's adoption of a low initial orbit is good and responsible strategy: if a satellite fails initial checks it can be readily de-orbited from such a low altitude and so does not add to the accumulation of space junk. However, it is a strategy that places the satellites at risk from space weather-driven changes in atmospheric drag, which is what happened to the ill-fated satellites launched on 3 February. The event clearly demonstrates one of several reasons why it is important to link responsible procedures to minimise space junk with space weather forecasting (Hapgood et al., 2022).

Several recent papers have studied the science behind this event. Fang et al. (2022) have looked at the CMEs causing the event, their propagation from Sun to Earth and their forecasting using the standard tools of a 3-dimensional MHD model of the heliosphere, based on solar magnetograph data, with a CME "cone model", which is inserted based on coronograph images of the event eruptions. It appears from this analysis that forecasts used by the SpaceX launch team underestimated the scale of thermospheric heating, and consequent density rises at the initial satellite orbit, that the event caused. For example, the standard empirical NRLMSISE-00 model (Picone et al., 2002) predicts a rise of only about 5% in neutral density at 210 km. Limb observations during the event indicate that the actual rise at 210 km was between 11% and 18% on the dusk side of the low-latitude Earth and 40% to 59% on the the dawn side (Y. Zhang et al., 2022). Dang et al. (2022) predict somewhat smaller rises in thermospheric densities than some other studies but show that the integrated effect on the satellites was still enough to cause re-entry from 210 km altitude. On the other hand, Kataoka et al. (2022) suggest the heating effect was greater and more widespread and the study by Tsurutani et al. (2022) of orbit changes from other satellites, such as Swarm, suggests the thermospheric density changes were large and the Starlink satellite orbits did not decay as fast as this would predict because they had been partially lifted from their initial orbit.

The thermospheric modelling by Dang et al. (2022) used the National Center for Atmospheric Research (NCAR) Thermosphere Ionosphere Electrodynamics General Circulation Model (TIEGCM), a three-dimensional, self-consistent, physical model of the coupled ionosphere-thermosphere system (Richmond et al., 1992). For very quiet times particle precipitation seems to dominate magnetospheric energy deposition in the ionosphere-thermosphere system; however, for small storms, the Joule heating by the ionospheric E-region Pedersen currents associated with F-region convection (X. Zhang et al., 2005; Kalafatoglu et al., 2018) is slightly larger than that due to particle precipitation, and for large storms Joule heating is dominant (Wilson et al., 2006; Robinson & Zanetti, 2021; Hajra et al., 2022). To define the Joule heating input to the coupled thermosphere-ionosphere model, Dang et al. (2022) employed the empirical convection and Joule heating model of Weimer (2005) which uses the prevailing solar wind and IMF conditions and assumes a steady-state response of the magnetosphere with only directly-driven energy deposition.

1.2 Polar cap Expansion and Contraction and Universal Time effects

In this paper, we look at the magnetospheric behaviour during the February 2022 events. In general, some of the energy extracted from the solar wind by the magnetosphere is directly deposited in the polar upper atmosphere by currents and precipitating particles, whereas a second component is stored in the geomagnetic tail and deposited after a delay (Baker et al., 1997; Shukhtina et al., 2005; Blockx et al., 2009; Liu et al., 2018). The energy is largely stored as magnetic energy of open flux in the tail and so the cycle of energy storage and release is reflected in the open flux, F_{PC}. However, F_{PC} is not a perfect indicator of energy stored because the lobe magnetic energy density is proportional to the square of the magnetic field in the lobe, which can be increased in the near-Earth tail for a given F_{PC} by the squeezing effect of enhanced solar wind dynamic pressure (Caan et al., 1973; Lockwood, McWilliams, et al., 2020; Lockwood, Owens, Barnard, Watt, et al., 2020). Nevertheless, because the ionospheric field B_i is effectively

constant, changes in the area of the region of ionospheric open flux (here termed the polar cap), $A_{PC} = F_{PC}/B_i$, indicate the energy storage in, and release from, the tail. The next section discusses the Expanding-Contracting Polar Cap (ECPC) model and how the expansion and contraction of the polar cap relates to ionospheric F-region convection voltages (Cowley & Lockwood, 1992; Lockwood & Cowley, 2022), and the associated E-region Pedersen currents and hence energy dissipation in the ionosphere and thermosphere by Joule heating. By using the ECPC model, in which the open flux rises and falls, we separate the energy deposition by the directly-driven system from that by the storage-release system, whereas if steady state is assumed (i.e., with constant F_{PC}) there is only directly-driven power dissipation and one is ignoring the existence of the storage-release system. There is not room here to review the literature on the relative importance of directly-driven and storage-release energy deposition in the ionosphere and thermosphere; however, we can say that both observations and global MHD modelling show that the storage-release system is certainly not negligible, is often dominant and cannot be ignored (Shukhtina et al., 2005; Blockx et al., 2009; Liu et al., 2018).

Another factor that we also investigate in the present paper is the effect on cycles of energy storage and dissipation of motions of the magnetic poles in any geocentric frame of reference, caused by Earth's rotation (Lockwood et al., 2021). These introduce Universal Time (UT) variations which are close to being in antiphase in the two hemispheres and which are larger in the southern hemisphere because the offset of the magnetic and rotational poles is greater. An often-discussed potential effect of pole motions on energy deposition is that of ionospheric conductivity variations. Enhanced conductivity, generated by solar EUV illumination, peaks when the polar cap is tipped towards the Sun whereas the pole-motion voltage effect peaks six hours earlier when the pole is tipping towards the Sun at its fastest rate. For the February period studied here, calculations of the mean conductivity in the northern polar cap and auroral ovals show almost no variation with UT as almost all of those regions is on the nightside (solar zenith angles, $\chi > 100°$) all of the time. On the other hand, there is a considerable quasi-sinusoidal UT variation in conductivity for the southern polar cap and auroral oval as most of those regions is subjected to diurnal variations in zenith angles χ below 90° that induce major conductivity changes (Ridley et al., 2004).

However, there are a number of points that need to be considered about effects of variations in this solar-EUV-induced conductivity in the polar cap and auroral oval. Much of the energy dissipation during geomagnetic storms takes place in the auroral ovals, caused by the Pedersen currents that connect the Region 1 and Region 2 field-aligned currents and where conductivity is dominated by auroral precipitation rather than being generated by solar EUV (Carter et al., 2020). This greatly reduces the significance of the solar EUV generated conductivity to energy deposition during geomagnetic storms. In addition, UT effects are introduced into heating rates by the neutral wind velocity (Cai et al., 2014; Billett et al., 2018), but we note that regular diurnal effects due to neutral winds are less clear in disturbed times when the convection pattern is changing faster than the neutral wind can respond.

There is also a need to be consistent when evaluating the roles of ionospheric conductivity and flux transport, a need that is imposed by Maxwell's equation $\nabla \cdot \mathbf{B} = 0$. The point being that this fundamental equation of electromagnetism (the non-existence of magnetic monopoles) demands that the open flux in the two hemispheres must be identical because it is generated and lost by magnetic reconnections which effect both hemispheres. In addition, when averaged over sufficient time, the antisunward magnetic flux transport rate of open flux in both ionospheric polar caps (i.e, the transpolar voltages) must be the same as that of the parts of the open field lines that are in interplanetary space. The latter cannot be influenced by ionospheric conductivity because the antisunward flow there is supersonic and super-Alfvénic. The same is true for most of the tail magnetosheath (Li et al., 2020). Several numerical simulations show that increased po-

lar cap conductivity reduces transpolar voltages (e.g., Borovsky et al., 2009). This is expected as field-perpendicular conductivities (both Hall and Pedersen) arise from collisions between ions and electrons and neutral atoms and ion-neutral collisions also give frictional drag on the motion of F-region plasma and frozen-in magnetic field (Ridley et al., 2004). As discussed by Tanaka (2007) and (for an isolated flux tube) by Southwood (1987), this is the "line-tying" concept introduced by Atkinson (1967, 1978) to explain the origin of field-aligned currents and how they transfer momentum and energy down into the ionosphere. Because the interplanetary segments of open field lines, outside the bow shock in the "Stern gap", and indeed in the tail magnetosheath, are flowing supersonically and super-Alfvénically away from the ionospheric polar cap that they are connected to, they can have no information about the state of the ionosphere and so are not influenced in any way by the slowing of their field line footpoints. Hence the reduction in transpolar voltage associated with enhanced polar cap conductivity must give induction effects in the field of the relevant tail lobe between the ionosphere and the tail magnetopause and hence a rise in the energy stored in that field. This means that enhanced conductivity is really influencing the balance between energy stored in the tail (and later released) and energy directly deposited in the ionosphere. Some (we will define it to be a fraction f_L) of the energy stored by the inductive field changes that decouple the ionospheric transpolar voltage and the Stern gap voltage, may be in in the tail antisunward of the reconnection X-line in the cross-tail current sheet that closes open flux: this part of the stored energy will be lost to the near-Earth magnetosphere and the ionosphere and returned to the solar wind. On the other hand, the remainder (a fraction $1 - f_L$) of the energy stored by the inductive field changes will be sunward of the tail reconnection X-line and that stored energy is deposited by Joule and particle heating via the storage-release system and in the ECPC, associated with the nightside reconnection voltage.

Because the resistance to motion of open field lines is in the ionosphere, almost all of any induced field changes and extra energy storage will be in the near-Earth magnetosphere and f_L will be very small. This means that if transpolar voltage in a given polar cap is reduced by enhanced polar cap conductivity (resulting in the associated directly-driven directly driven energy deposition in the ionosphere and thermosphere being reduced), after a short delay (typically a substorm growth duration) the lost energy is deposited by the flows and associated Joule heating accompanying the enhanced nightside reconnection as part of the storage-release system. Hence "saturation" effects associated with enhanced ionospheric conductivity which limit the transpolar voltage and Joule dissipation (X. Zhang et al., 2005) do not cause a reduction in total flux transport seen in the ionosphere, but they do spread it out over a longer time interval via the storage/release system and this will have a corresponding effect on the variation in Joule heating. Hence if we were to include modulation of the directly-driven transpolar voltage by ionospheric EUV-generated conductivity effects, we would also need to modulate the storage-release system in an appropriate way which requires knowledge of the tail lobe field changes.

In theory, this can be achieved using a full global MHD model of the magnetosphere, but here we do not include EUV-induced conductivity effects on transpolar voltage in the summer (southern) hemisphere because to modulate the directly-driven system without including a matching modulation of the storage-release system would be an inconsistent analysis. In addition, we argue that for the dominant energy deposition in the auroral oval, conductivity induced by particle precipitation dominates over that due to solar EUV photoionization.

2 Theory and Methods

2.1 Polar cap Expansion and Contraction

Two key parameters in the analysis presented in this paper are the dawn-dusk diameters of the ionospheric polar caps, d_{PC}, and the voltage placed across them by the

solar wind flow, the transpolar voltage, Φ_{PC} (also referred to as the cross-cap potential drop and synonymous with the polar cap flux transport rate). We investigate the variation of both using the Expanding-Contracting Polar Cap (ECPC) model (Cowley & Lockwood, 1992; Lockwood & Cowley, 2022). Continuity of open flux is the core equation of the ECPC model and is equivalent to Faraday's law (in integral form) applied to the open-closed field line boundary:

$$dF_{PC}/dt = \Phi_D - \Phi_N \tag{1}$$

where F_{PC} is the magnetospheric open flux, Φ_D is the reconnection voltage in the dayside magnetopause (the rate of production of open flux) and Φ_N is the reconnection voltage in the nightside, cross-tail current sheet (the rate of loss of open flux).

We here adopt the major simplifying assumption that the ionospheric open-flux polar caps remain circular. This is certainly not valid all of the time, particularly for strongly and prolonged northward IMF when F_{PC} is well below its average value of about $0.4GWb$. In such cases, a "horse-collar" auroral form is often seen, indicating a teardrop-shaped open flux region (Hones et al., 1989; Elphinstone et al., 1993; Imber et al., 2006; Milan et al., 2020; Bower et al., 2022; Wang et al., 2022). Nevertheless, the assumption of a circular polar cap has been successfully used many times with the ECPC model (e.g., Lockwood et al., 1990; Milan et al., 2017), including an analysis of a full year of data (Milan et al., 2021) and has two major advantages for the present study. Firstly the transpolar voltage is given by (Lockwood, 1991; Connor et al., 2014; Milan et al., 2017, 2021)

$$\Phi_{PC} = (\Phi_D + \Phi_N)/2 + \Phi_V \tag{2}$$

where Φ_V is the sum of the voltages induced by all viscous-like (non-reconnection) mechanisms. Secondly this assumption allows us to relate the flux F_{PC} and diameter d_{PC} of the polar cap. We use Equation 4 of Milan et al. (2021) which they employ to derive the open flux F_{PC} by integration of the vertical ionospheric field B_i inside the polar cap from the latitude of the region 1 field-aligned currents using a model geomagnetic field with an offset of the circular polar cap centre towards the nightside of 4° . These authors find the values F_{PC} are insensitive to this offset in the range 1° -10°. We remove the latitudinal offset of $\Delta\Lambda = 4°$ between the open-closed boundary and the region 1 currents that Milan et al. employed and express the latitudinal radius in terms of the open flux polar cap diameter, an arc length, d_{PC} at an altitude of $400km$:

$$F_{PC} = (3.259\times10^{-5})d_{PC}^2 + 23.53d_{PC} - (2.7\times10^7) \tag{3}$$

where F_{PC} is in Wb and d_{PC} is in m .

Note that subtle changes in the shape of the open polar cap are a key part of understanding the pattern of ionospheric convection, as predicted by the ECPC model (Lockwood & Morley, 2004), particularly in determining the pattern of flow following a burst in either the magnetopause or the tail reconnection voltages. However, the distortions to the boundary, and the flow patterns associated with them, propagate around the boundary (Morley & Lockwood, 2005). These transient features, and others associated with filamentary field-aligned currents caused by dynamic pressure pulse impacts on the magnetosphere (Lühr et al., 1996), are therefore not part of the present paper because of the simplifying assumption of a circular polar cap.

When using the ECPC it is important to understand the importance of the timescale τ over which the data are averaged. If a large τ is used, this is averaging over many cycles of expansion and contraction of the polar cap and dF_{PC}/dt tends to zero. From Equation 1 this steady-state condition means that $\langle\Phi_N\rangle_\tau = \langle\Phi_D\rangle_\tau$. Only for small τ do we

see the full expansion and contraction of the polar cap. Increasing τ causes the analysis to tend towards steady state. An important timescale in this is $\tau \sim 1hr$, which is close to the average duration of the substorm cycle. In such cycles, although much of the open flux generated in the growth phase (by enhanced magnetopause reconnection voltage Φ_D) can be lost in the subsequent expansion and recovery phases by enhanced reconnection voltage in the cross-tail current sheet, Φ_N, one substorm cycle does not generally return the polar cap flux to the value it had at the start of the growth phase. It can take a string of weakening substorm expansions to achieve that (Lockwood & McWilliams, 2021b). Conversely, some substorms deposit more energy than was stored in the growth phase leaving the stored tail energy at a lower level that it was at the start of that growth phase (Baker et al., 1997). Furthermore there are steady convection intervals (Lockwood et al., 2009) and intervals of driven convection (Milan et al., 2021) which can last considerably longer than an hour. Later in this paper we demonstrate that the first CME in the February 2022 event is an example of how large, persistent and increasing Φ_D prevents Φ_N establishing a steady-state, despite several substorm expansions, even on averaging timescales of 1-2 days. In general, the voltage Φ_D is constantly changing because of the variability in the solar wind parameters (Lockwood, Bentley, et al., 2019; Lockwood, 2022; Lockwood & Cowley, 2022). As a result, although steady state is a good approximation for τ of several days, we can still detect the effects of non-steady behaviour at $\tau = 1hr$, although they will be reduced in magnitude by the averaging.

Lockwood and McWilliams (2021b) used a dataset of 25 years of hourly-averaged data ($\tau = 1hr$) to show that the optimum solar wind coupling function depends on which magnetospheric response index it is aimed at predicting. In particular, they showed that the coupling function that best predicts transpolar voltage Φ_{PC} is considerably different from those that best predict geomagnetic activity indices. Best practice in deriving these coupling functions was discussed by these authors and by Lockwood (2022). In particular, the results of regression and correlation analysis tends to be weighted towards the means of the distributions and the fit often underestimates the full range and extreme values of the observations (Lockwood et al., 2006; Sivadas & Sibeck, 2022). The method used by Lockwood and McWilliams (2021b) and Lockwood (2022) avoids this by fitting to averages in bins that cover the full range, meaning that the weighting is equal across the whole range of the data and not dominated by the larger number of data points close to the mean. There are also pitfalls over time resolution (Laundal et al., 2020; Lockwood, 2022). Figure 1 demonstrates the best-fit coupling function to the transpolar voltage observed by the SuperDARN coherent radar network and shows that another major pitfall, overfitting, has been avoided because the fit is essentially the same for the independent test half of the dataset than for the fit data subset that was used in the derivation of the coupling function. Overfitting is a problem that is particularly facilitated by the presence of datagaps in the interplanetary data which were a serious but neglected problem for coupling function studies using data from before the advent of the near-continuous data from the ACE and Wind interplanetary monitors in 1995. The best way to handle data gaps has been discussed by Finch and Lockwood (2007) and Lockwood, Bentley, et al. (2019). In both cases shown in Figure 1, an optimum lag of $20min$ of Φ_{PC} behind the interplanetary coupling function is employed (see Figure 6 of Lockwood & McWilliams, 2021b).

The mauve line in Figure 1 is an average fit to many years of data, which means that steady-state applies to the fitted value so that, from Equation 2, $\langle \Phi_D \rangle = \langle \Phi_N \rangle = \langle \Phi_{PC} - \Phi_V \rangle$. The best-fit is given by:

$$\langle \Phi_{PC} \rangle = \langle \Phi_D \rangle + \langle \Phi_V \rangle = s_T [B_\perp^a \rho_{sw}^b V_{sw}^c sin^d(\theta/2] + i_T \qquad (4)$$

where: $B_\perp = (B_Y^2 + B_Z^2)^{1/2}$ is the IMF transverse to the X direction of the Geocentric Solar Magnetospheric (GSM) frame (in nT); ρ_{sw} is the solar wind mass density

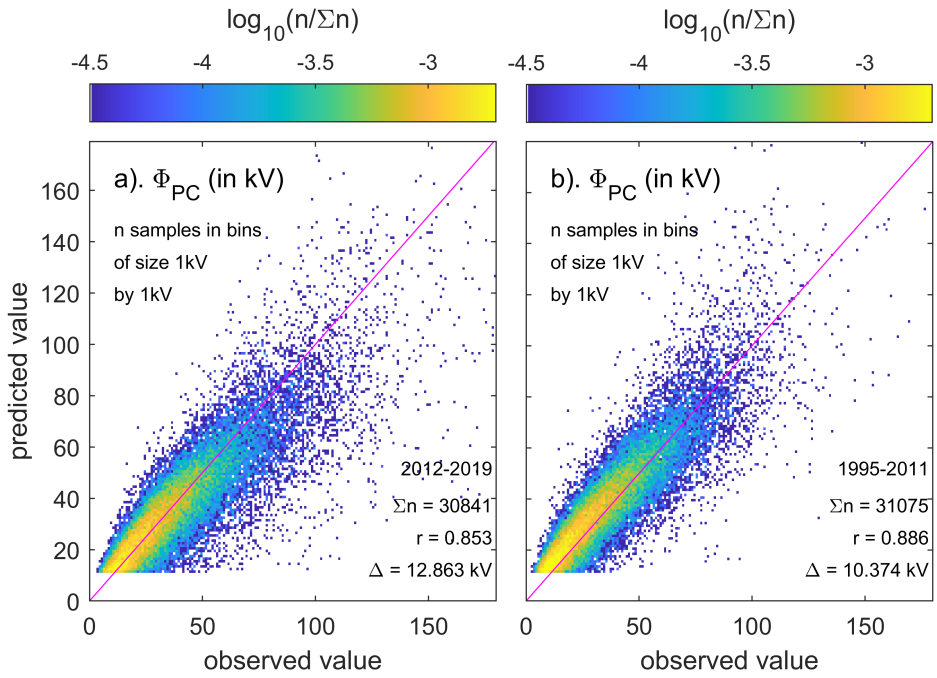

Figure 1. Scatter plots of observed and predicted hourly means of transpolar voltage, Φ_{PC}. The observations are from the survey of 25 years' data from the northern hemisphere coherent-scatter SuperDARN radar network by Lockwood and McWilliams (2021b). The predicted values are made using the interplanetary data in the Omni2 dataset (King & Papitashvili, 2005), using the procedure described by Lockwood and McWilliams (2021a) to generate a coupling function for transpolar voltage (see Equation 4 of text). (a) is for the fit data subset (2012-2019, inclusive) and (b) for the independent test data subset (1995-2011, inclusive). In both panels the fraction of valid samples, $n/\Sigma n$, is color-coded on a logarithmic scale as a function of observed and predicted transpolar voltage, in bins of size $1kV$ by $1kV$ with $n \geq 3$ samples. The total number of samples, Σn, the correlation coefficient, r, and the r.m.s. deviation of fitted from observed values, Δ, are given. The mauve line are perfect agreement of observed and predicted Φ_{PC}.

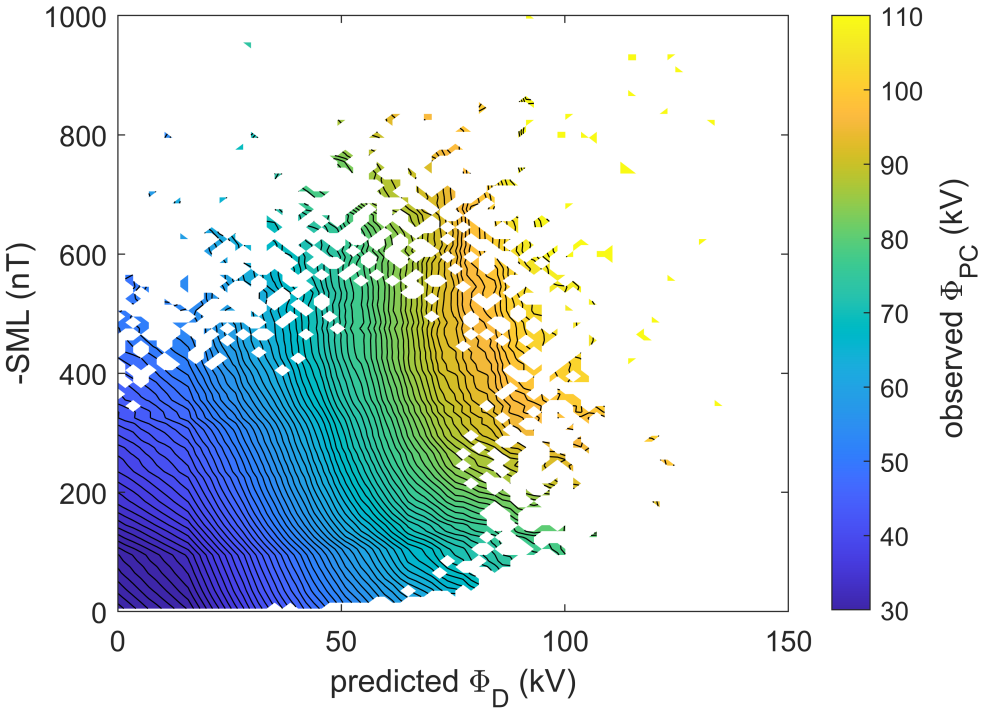

Figure 2. Contours of hourly means of transpolar voltage, Φ_{PC}, as a function of the predicted magnetopause reconnection voltage from Equation 2, Φ_D, and -*SML*. The observations are from the same survey of 25 years' data as Figure 1.

(in kg cm^{-3}); V_{sw} is the X-component of the solar wind velocity (in km s^{-1}), $\theta = tan^{-1}(|B_Y|/B_Z)$ is the IMF clock angle in the GSM frame and B_Y and B_Z are the Y and Z IMF components in that frame. The best-fit constants are a =0.6554, b =0.0522, c =0.6676, d =2.5, i_T =13.5kV and s_T =8.4075 for the above parameter units and Φ_{PC} in kV. Given that the viscous-like voltage is not predicted to have the dependence on the IMF clock angle, we here take Φ_V to be equal to i_T = 13.5kV, a value reasonably consistent with studies by both ground-based radars and satellite observations at the flank magnetopause (Lockwood & McWilliams, 2021b; Hapgood & Lockwood, 1993). Hence

$$\Phi_D = s_T[B_\perp^a \rho_{sw}^b V_{sw}^c sin^d(\theta/2)] \quad (5)$$

Equation 5 is derived from hourly means. We studied the relationship between the 1-minute values of Φ_D and a variety of one-minute geomagnetic indices (*SML*, *SMU*, *AL*, *AU*, *SMR* and *SYM-H*) at the optimum lag and compared it with that for 1-hour running means of the same data. The correlation is naturally lower for the 1-minute data in each case as the scatter is greater, but the best-fit polynomial is almost identical for the two time resolutions in all cases. Hence we here use Equation 5 to generate 1-minute values of Φ_D. We employ a lag of $\delta t = 5min$ between the interplanetary observations (which are propagated from L1 to the bow shock) and Φ_D, that being the lag derived by (Lockwood & McWilliams, 2021b) between the hourly means of Φ_{PC} and running hourly means of the coupling function from IMF data when auroral electrojet activity was quiet ($-AL \leq 100nT$).

A different analysis of the same dataset reveals that much of the scatter in Figure 1 is caused by a mechanism other than dayside magnetopause reconnection. Figure 2 shows contours of observed transpolar voltage Φ_{PC}, from the same dataset, as a function of hourly means of the predicted lagged magnetopause reconnection voltage from Equation 2, Φ_D, and the SuperMAG *SML* index. This index is constructed in the same way as the *AL* index but uses many more stations in the northern hemisphere (of order 100 instead of the ring of 12) and so avoids the non-linear effect in *AL* caused by polar cap expansion to equatorward of the ring of 12 stations (Gjerloev, 2012; Newell & Gjerloev, 2011). Because, like *AL*, *SML* is increasingly negative with enhanced activity we here use *-SML* in plots and descriptions.

The key point to note about Figure 2 is that the contours slope diagonally across the plot. This means that at a given predicted Φ_D the transpolar voltage Φ_{PC} increases with increasing *-SML*. This is true in all regions of this parameter space except when both Φ_D and *-SML* are very large when the contours become vertical showing that Φ_{PC} is then a function of Φ_D only. Thus even using hourly data we can detect an influence on transpolar voltage which depends on the auroral electroject activity level. This is therefore a separate influence on the transpolar voltage, as predicted to be supplied by Φ_N in the ECPC model. The same picture emerges from the Active Magnetosphere and Planetary Electrodynamics Response Experiment (AMPERE) analysis of data on field-aligned currents from magnetometers on board more than 70 Iridium satellites in circular low-Earth orbit (altitude 780 km) in 6 orbit planes, which give 12 cuts at different MLTs in each orbit through the auroral oval (Anderson et al., 2014; Milan et al., 2015): from Chree analysis of these data, Milan et al. (2018) show that the field-aligned currents that bring convection circulation of the magnetosphere down to the ionosphere are enhanced in response both to a coupling function that quantifies dayside magnetopause reconnection and also to the $-AL$ index.

The problem in applying the ECPC is that the the nightside reconnection voltage Φ_N is hard to quantify (Walach et al., 2017; Øye, 2018). Several studies have used Equation 1 to infer it from the rate of change of open polar cap flux dF_{PC}/dt and the value of Φ_D deduced from interplanetary parameters using a coupling function of the type given by Equation 5. For example, Grocott et al. (2002) used dF_{PC}/dt deduced from the bite-out in the nightside polar cap in a substorm expansion phase observed by magnetometers, radars and imagers. The same basis was used by Milan et al. (2007), Øye (2018) and Milan et al. (2021) using the circular polar cap assumption and looking at the change in radius of the polar cap inferred from global auroral images or the locations of field-aligned current sheets deduced from the AMPERE programme. This method is not useful here where we wish to use Φ_N to predict the variation of F_{PC}. The way forward was first established by Holzer et al. (1986) who used the *AL* nightside auroral electrojet index as a proxy for Φ_N to study two polar cap expansions and contractions using Equation 1. The validity of this approach has been confirmed by several studies of larger datasets, including the statistical survey of 25 years of data by Lockwood and McWilliams (2021b) who found that transpolar voltage was a function of Φ_D with an independent influence related to *AL*, something we have demonstrated here with Figure 2 using the SuperMAG *SML* index in place of *AL*. This confirms *SML* can be used as a basis for the quantification of Φ_N.

The mauve line in part (a) of Figure 3 is a polynomial fit to all the hourly means of Φ_{PC} from the survey of Lockwood and McWilliams (2021b) as a function of the simultaneousigmas hourly means of *-SML*. There is considerable spread in the data which we expect for two known reasons: firstly Φ_D contributes to Φ_{PC} as well as Φ_N, and secondly there are ionospheric conductivity and other seasonal effects in the relationship between Φ_{PC} and the geomagnetic *SML* index. Part (b) of Figure 3 shows the equivalent plot for strongly northward IMF ($[B_Z]_{GSM} \geq 10nT$) when we can take Φ_D to be zero. The mauve line is the same as in part (a) and remains a good fit to the average

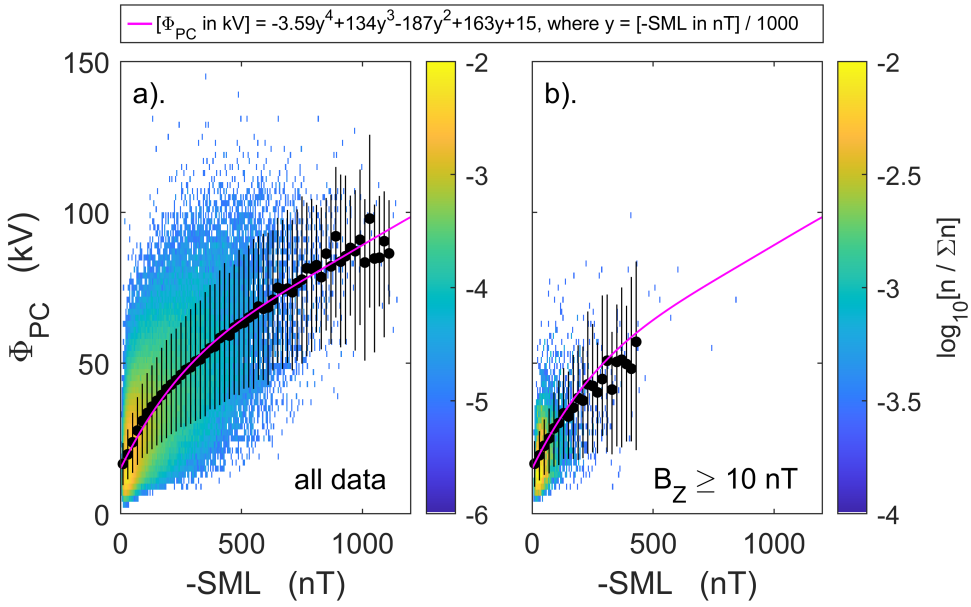

Figure 3. Scatter plots of observed hourly means of transpolar voltage, Φ_{PC} as a function of -*SML*, where *SML* is the SuperMAG auroral electrojet index. The observations are from the survey of 25 years' data from the northern hemisphere coherent-scatter SuperDARN radar network by Lockwood and McWilliams (2021b). Both panels are for the full data set (1995-2019, inclusive); (a) is for all data and (b) for the subset of strongly northward IMF with $B_Z \geq 10nT$, lagged by the optimum delay between B_Z and Φ_{PC} of $\delta t = 18min$. In both panels the fraction of valid samples, $n/\Sigma n$, is color-coded on a logarithmic scale as a function of observed *SML* and Φ_{PC}, in bins of size $5nT$ by $2kV$. As in Figure 1, only bins containing 3 or more samples are coloured. Also shown are the mean Φ_{PC}, with error bars between the 15.9% and 84.1% of the cdf (1-σ points), for bins in *SML* $20nT$ wide in which there are 25 or more samples. The mauve lines in both panels is the best polynomial fit to the mean values in (a), given at the top of the Figure.

data, which covers a smaller range of both Φ_{PC} and *SML*, as expected for northward IMF. However, although the scatter is reduced because Φ_D is not a factor, it is still considerable.

To estimate the contribution to Φ_N of processes associated with the substorm current wedge, we adopt the fitted form to Φ_{PC} as a function of *SML* (given at the top of Figure 2) but scale it with a factor $k(F)$, that is a function of time of year, F, to allow for the seasonal effects in these northern hemisphere radar and magnetometer data. This gives us an estimate of the tail reconnection rate associated with auroral electrojet activity, as quantified by *SML*:

$$[\Phi_{N1} \quad in \quad kV] = k(F) \times f(SML) = k(F) \times [-3.59y^4 + 134y^3 - 187y^2 + 15] \tag{6}$$

where y = [-*SML* in nT].

However, the scatter in Figure 3b shows that *SML* does not uniquely define Φ_N. The same conclusion can be drawn from the survey of 1-year of data by Milan et al. (2021) in which the ratio Φ_N/SML appears to be different, on average, for different phases of magnetospheric behaviour. On the other hand, Milan et al. (2007) show that almost all Φ_N occurs soon after bursts in Φ_D and a base-level of Φ_N between events was not detected. However, we note that the viscous-like voltage Φ_V may well actually be due to low-level continuing Φ_N because ongoing unbalenced nightside reconnection has the ability to mimic all the ionospheric flows that have been attributed to viscous-like interaction.

For reasons explained below, we propose that in addition to Φ_{N1} (which is associated with enhanced -*SML*), there is a second, quasi-steady component of tail reconnection associated with magnetic shear across the cross-tail current sheet (and hence related to the open flux F_{PC}) but which does not register in *SML*, such that

$$\Phi_N = \Phi_{N1} + \Phi_{N2} \tag{7}$$

We take this additional loss of F_{PC} to be linear with a time constant t_N

$$\Phi_{N2} = F_{PC}(\delta t)/t_N \tag{8}$$

where δt is the lag to allow for the propagation of open flux into the tail after its generation (at rate Φ_D). We here use $\delta t = 15$ min., the derived optimum lag between the predicted Φ_D and observed Φ_{PC} in the study by (Lockwood & McWilliams, 2021b, -see their Figure 6). We repeated our analysis for $\delta t = 10min$ and $\delta t = 30min$ and found only small changes to our results. Note that there is a potential improvement we could make to Equation 8 in that the rate could be made a function of solar wind dynamic pressure p_{SW} and the dipole tilt angle δ as there are observations that indicate that, together, they influence the rate of nightside reconnection by squeezing the tail (Schieldge & Siscoe, 1970; Caan et al., 1973; Kokubun et al., 1977; Karlsson et al., 2000; Finch et al., 2008; Hubert et al., 2009; Yue et al., 2010; Lockwood, 2013; Lockwood, McWilliams, et al., 2020; Lockwood, Owens, Barnard, Watt, et al., 2020; Lockwood et al., 2021). This would not influence the voltage Φ_{N1} as it would also raise *SML* from which it is computed; however, it would influence Φ_{N2}. However, variations in p_{SW} have also been proposed to influence Φ_D, field aligned currents and Joule heating (Lukianova, 2003; Lee, 2004; Palmroth, 2004; Boudouridis, 2005; Stauning & Troshichev, 2008): hence, there is a danger in including solar wind dynamic pressure effect in one area and not another.

To ensure that we are not inconsistent in the present analysis we do not include the effects of p_{SW} variations in the present analysis. However, we do highlight times when changes in p_{SW} may have had an effect.

The reason for proposing a second component of Φ_N that does not depend on *SML* is that without it during the events studied F_{PC} grows to either unrealistic values (exceeding $2.5GWb$) and/or falls to below zero for any $k(F)$.

To compute the scaling factor $k(F)$, for the time of year F of the events (early February) we make use of the fact that averaged over a long enough period τ, the means $\langle\Phi_D\rangle_\tau$ and $\langle\Phi_N\rangle_\tau$ become equal and hence steady-state applies (and by Equation 2, the polar cap flux is constant). Choosing the interval τ needed, however, is a compromise between two factors: if τ is too large the seasonal variation between Φ_N and *SML* becomes a factor but if is is too short (less than a couple of days) then steady-state is not achieved. We searched the data around the events of interest and found two times that were of order one week apart for which both the predicted Φ_D (from Equation 1) and observed -*SML* were very low (below $1kV$ and $20nT$, respectively) and followed intervals of at least 1 day when Φ_D and -*SML* had remained low. Two such times around the events of interest were UT = 11 hrs of day-of-year (d-o-y) 30 and UT = 5 hrs on d-o-y 38, giving an interval of duration τ of 7.75 days. We will refer to this as the "calibration interval". From Equations 1, 6, 7 and 8

$$dF_{PC}/dt = \Phi_D - k(F)\times f(SML) - F_{PC}(\delta t)/\tau_N \tag{9}$$

Equation 9 has two unknowns, $k(F)$ and τ_N - but for given values of these two parameters we can compute the variation of F_{PC} from the known variations of Φ_D and *SML*. We start these computations for a wide range of initial values of F_{PC} at the start of doy 1 of 2022 and we find that this initial condition has no effect on the variation after d-o-y 30. For a given τ_N, we iterate $k(F)$ until F_{PC} at the end of the calibration interval equals that its start. This means that the integral of Φ_D over the interval equals the integral of Φ_N and steady state is achieved over this timescale.

If τ_N is too small F_{PC} becomes negative. If τ_N is too large we find F_{PC} reaches peaks larger than the largest values that have been detected, which are near $1GWb$ (Boakes et al., 2009; Milan et al., 2021) . We find that this F_{PC} is reached in both the peaks in the event studied here for $\tau_N = 6.8min$. Section 4 provides evidence that it is an appropriate value for τ_N.

2.2 Universal Time effect: polar cap motions

A series of 4 papers Lockwood, Owens, Barnard, Haines, et al. (2020); Lockwood, McWilliams, et al. (2020); Lockwood, Owens, Barnard, Watt, et al. (2020); Lockwood et al. (2021) have investigated the semi-annual and Universal Time (UT) variations in the magnetosphere and in geomagnetic activity. The last of this series brings the conclusions together and successfully models the UT (and annual) variations of observed hemispheric geomagnetic indices by introducing a key component that had been hitherto overlooked. The interplanetary electric field is measured by spacecraft in geocentric frames, such as GSM, GSE or GSEQ, i.e. frames that are fixed in relation to the centre of the Earth. Because Earth's magnetic poles are offset from the rotational poles, the magnetic poles and the ionospheric polar caps move in this frame in a diurnal circle. Both observations (Stubbs et al., 2005) and geomagnetic field modelling (Tsyganenko, 2019) of the auroral oval show that the polar cap moves with its magnetic pole with very little change in shape.

There are a number of observations relevant to these diurnal motions of the polar cap caused by Earth dipole tilt. Newell and Meng (1989) surveyed 3 years' data from

the DMSP (Defense Meteorological Satellite Program) F7 satellite and showed that the region of solar wind precipitation in the cusp region migrated in geomagnetic latitude by about 0.06° for each 1° shift in dipole tilt angle. That means that (94%) of the motion of the magnetic pole in a geocentric frame is reflected in the cusp location and only 6% in the geomagnetic frame. The cusp precipitation is on newly-opened field lines generated by the voltage Φ_D (see review by Smith & Lockwood, 1996) and hence this dipole-tilt induced motion of the dayside open-closed boundary (OCB) in a geocentric frame mainly reflects that in the magnetic pole. Similarly on the nightside, Vorobjev and Yagodkina (2010) showed that the magnetic latitude of the poleward edge of the nightside northern-hemisphere auroral oval, as detected in DMSP satellite data from 1986, had a sinusoidal diurnal variation in amplitude near 2°, whereas the offset of the rotational northern eccentric axial pole at that time was about 8°. Hence in a geocentric frame only about 75% the motion in the magnetic pole is reflected in this boundary. However, this boundary is generally equatorward of the nightside OCB and this is likely to make this percentage a poor estimate of the real value that would apply to the nightside OCB. The magnetic field tracing needed by global MHD model of the magnetosphere means that the OCB can be identified in simulations and Kabin et al. (2004) found that magnetic latitude shifts in the noon OCB were 1.3° and −0.9° for dipole tilts of +35° and −35°, i.e., 3.9% and 2.7%, respectively. The corresponding shifts in the midnight OCB were 0.8° and −0.5° (2.3% and 1.5%, respectively). Hence these simulations show the nightside OCB moves even more closely with the magnetic pole than the dayside OCB. The fact that the OCB is largely moving with the geomagnetic poles shows that closed field lines outside the open field line region are also taking part in this diurnal wobble caused by the pole motion. Oznovich et al. (1993) showed that during low auroral activity, the auroral oval as a whole was shifted by 1° in geomagnetic coordinates for every 10° change in the dipole tilt angle (90%). Being at large longitudinal separations (if not exactly the 180° for a geocentric dipole model) the motion of the auroral ovals induced by the magnetic pole motions would be close to, but not exactly, in antiphase in a geocentric frame with the southern pole moving antisunward when the northern is moving sunward, and *vice-versa*. This was directly observed by (Stubbs et al., 2005), using full and simultaneous auroral images of the northern and southern auroral ovals made by the IMAGE and Polar satellites.

The speeds of these motions of the polar cap in a geocentric frame are very much smaller than that of the solar wind: in the northern hemisphere the sunward speed of motion V_{NP} is a sine wave of amplitude $57ms^{-1}$, but the larger offset of the southern magnetic pole from the rotational pole makes the corresponding amplitude of the speeds there, V_{SP} about $135ms^{-1}$. These values were computed using the the eccentric dipole field model of the geomagnetic field by Koochak and Fraser-Smith (2017) by Lockwood et al. (2021). However, in the ionosphere the magnetic field B_i is approximately $5{\times}10^{-5}T$, which is much greater than the flow-perpendicular field in interplanetary space (which is typically $5nT$). The diurnal motion toward and away from the Sun induces an electric field across the northern polar cap in a geocentric frame of $V_{NP}B_i$ and a voltage in that frame across the polar cap of $\phi_{MN} = V_{NP}B_i d_{PC}$, where d_{PC} is the polar cap diameter. Using a typical polar cap angular radius of 15° gives $d_{PC}{\approx}3.6{\times}10^6 m$ and a sinusoidal diurnal voltage variation of amplitude $10kV$. In the southern hemisphere, the larger offset of the poles means that this amplitude is $24kV$. Note the importance here of the eccentric dipole model. Use of a geocentric dipole makes every effect on the north pole motion equal and opposite to that of the south pole. Hence for a geocentric dipole, although Earth's rotation alternately causes a given effect in one hemisphere and then the other, the global effect (the sum of the two) is always zero. This is not the case for an eccentric dipole.

These effects of pole motions, like the conductivity-induced changes discussed earlier, change the balance between directly-deposited energy and energy stored in the tail and then deposited via the storage-release system. Let us consider the Northern polar

cap: when it is moving sunward (with a velocity $V_{NP} > 0$ that peaks at around 12 UT) the antisunward convection in the polar cap in a geocentric frame will be reduced by the motion of the cap as a whole (i.e. by V_{NP}) and the voltage across the cap in that frame will be reduced by $\phi_{MN} = V_{NP} B_i d_{PC}$, even if the reconnection voltages Φ_D and Φ_N are unchanged. The convection pattern perturbations for sunward/antisunward motions of the polar cap as a whole (and dawnwad/duskward motions) were sketched by (Lockwood, 1991). This means the directly-deposited Joule heating is reduced. In a geocentric frame, the flux transfer rate over the northern ionospheric polar cap is reduced to $\Phi_{PC} - \phi_{MN}$ but, given that the voltage across the region of open field lines in interplanetary space is unchanged, this means that flux is accumulating in the northern lobe at a rate that is ϕ_{MN} greater than it would have done if V_{NP} had been zero. Conversely, in the other 12-hour phase of the diurnal cycle the transpolar voltage is enhanced because V_{NP} and ϕ_{MN} are negative and the rate of flux storage in the tail lobe is reduced. Hence the transpolar voltage in the northern polar cap is

$$\Phi'_{NC} = \Phi_{PC} - \phi_{MN} = \Phi_{PC} - V_{NP} B_i d_{PC} \tag{10}$$

and in the southern hemisphere

$$\Phi'_{SC} = \Phi_{PC} - \phi_{MS} = \Phi_{PC} - V_{SP} B_i d_{PC} \tag{11}$$

where V_{NP} and V_{SP} are the sunward components of motion of the northern and southern polar caps.

If the variations of V_{NP} and V_{SP} were of the same amplitude and in antiphase then although there would be more power deposited in the northern polar cap (and/or stored in the northern tail lobe) for half the day, and then more in the southern hemisphere for the other half so that the sum of the two would be constant. However these motions are not of equal amplitude, nor are they exactly in antiphase and this leaves a net UT variation in power deposited or (stored in that tail) globally (Lockwood et al., 2021).

Note that the magnetospherically-imposed voltage Φ_{PC} across the polar caps of the two hemispheres can be different at any one instant of time because of different inductive changes in the magnetic fields of the two tail lobes. However, on average they must be the same: by Faraday's law, a voltage is synonymous with a magnetic flux transfer rate and maintaining $\nabla \cdot \mathbf{B} = 0$ means that the long-term average of flux transport over the south pole must equal that over the north pole. In in other words $\langle \Phi_{PC} \rangle$ must be the same in the two hemispheres. A number of statistical studies of satellite data report differences in the long-term averages of the transpolar voltage in the two hemispheres (e.g., Förster & Haaland, 2015) which almost certainly reflect aliasing of orbit paths with seasonal, UT and solar cycle variations.

3 The February 2022 event

Figure 4 shows the variations of various geomagnetic activity indices during the events of early February 2022. The gray bands mark the times of the CME passages past the Earth, as defined from interplanetary data by Dang et al. (2022). The top panels shows the 3-hourly planetary range indices, *am*, *an*, and *as* with peaks near the ends of each of the CME events. Both peaks reach $86nT$ in the global *am* index. The variations of the hemispheric sub-indices, *an*, and *as*, are very similar to that for *am*. Panel (b) shows large enhancements in the nightside auroral electrojet index -*SML* at the times of the peaks in *am*. The bottom panel shows the *SMR* and *SYM-H* indices compiled from low-latitude stations and mainly responding to the ring current. These show intensifications that peak shortly after the peaks in -*SML* but which decay more slowly.

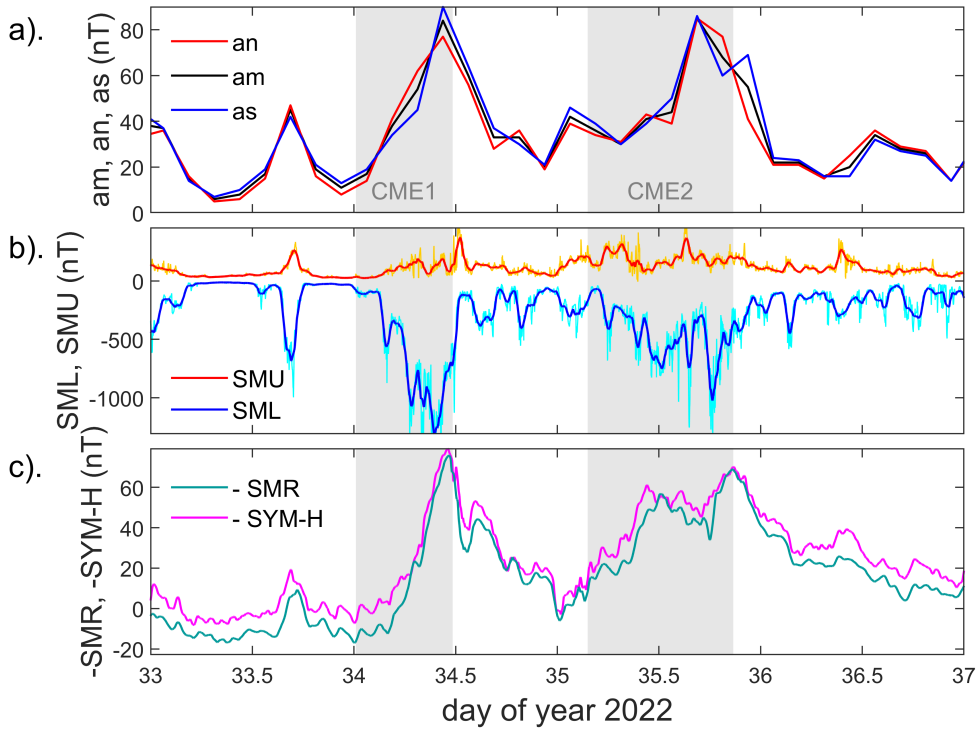

Figure 4. Geomagnetic indices during the events of 3-4 February 2022. Plots are for 00 UT on 2 February (d-o-y 33) to 00UT on 6 February (d-o-y 37). The grey bands mark the times of the passages of the two CME events at Earth's bow shock, as identified by Dang et al. (2022). (a). The mid-latitude range *am* index (in black) with its northern and southern hemisphere components, *an* (in red) and *as* (in blue). (b). The SuperMAG SMU (red/orange) and SML (blue/cyan) auroral electrojet indices: the orange and cyan lines are the $1min$ values and the red and blue lines are $20min$ running means of those 1-min. data. (c). $20min$ running means of the *SMR* and *SYM-H* indices. .

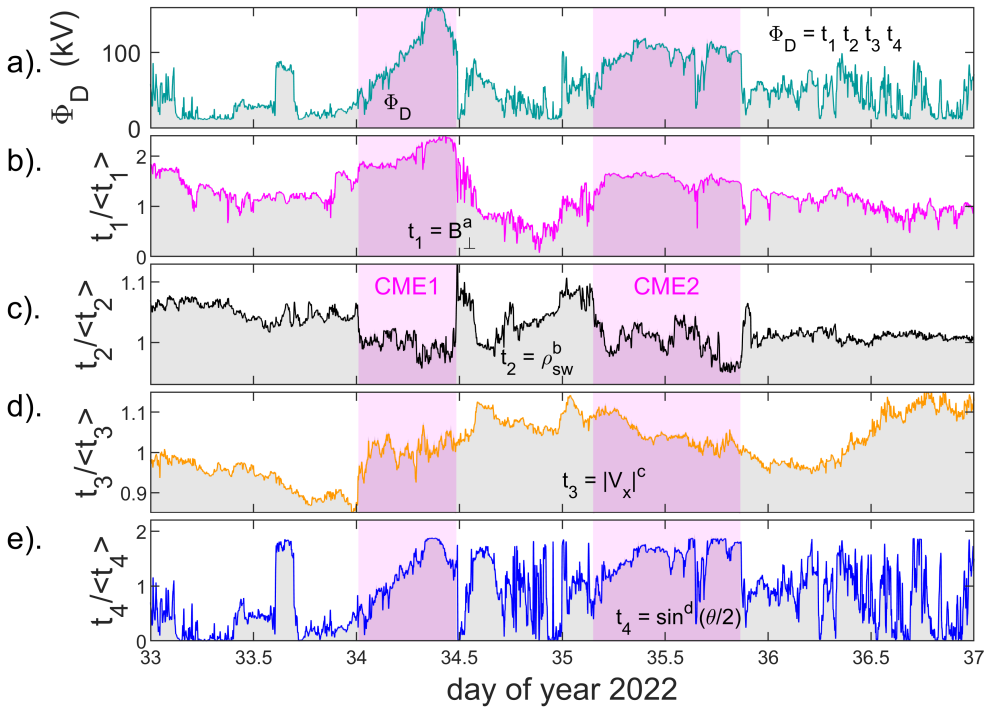

Figure 5. Variations of 1-minute integrations of solar wind parameters during the interval shown in Figure 4. Panel (a) shows the derived magnetopause reconnection voltage Φ_D, given by Equation 5, and the panels beneath show the component terms, normalised to their mean value in the interval. (b). $t_1 = B_\perp^a$ where $B_\perp = (B_Y^2 + B_Z^2)^{1/2}$ is the IMF transverse to the X direction of the Geocentric Solar Magnetospheric (GSM) frame in which the Y and Z components are B_Y and B_Z. (c). $t_2 = \rho_{SW}^b$ where ρ_{sw} is the solar wind mass density. (d). $t_3 = V_{SW}^c$ where V_{sw} is the X-component of the solar wind velocity. (d). $t_4 = sin^d(\theta/2)$ where $\theta = tan^{-1}(|B_Y|/B_Z)$ is the IMF clock angle in the GSM frame . The best-fit exponents are $a = 0.6554$, $b = 0.0522$, $c = 0.6676$, $d = 2.5$. The vertical pink bands show the times of the CME passages. All parameters are lagged by the inferred propagation time to the dayside ionosphere of $\delta t = 5min$.

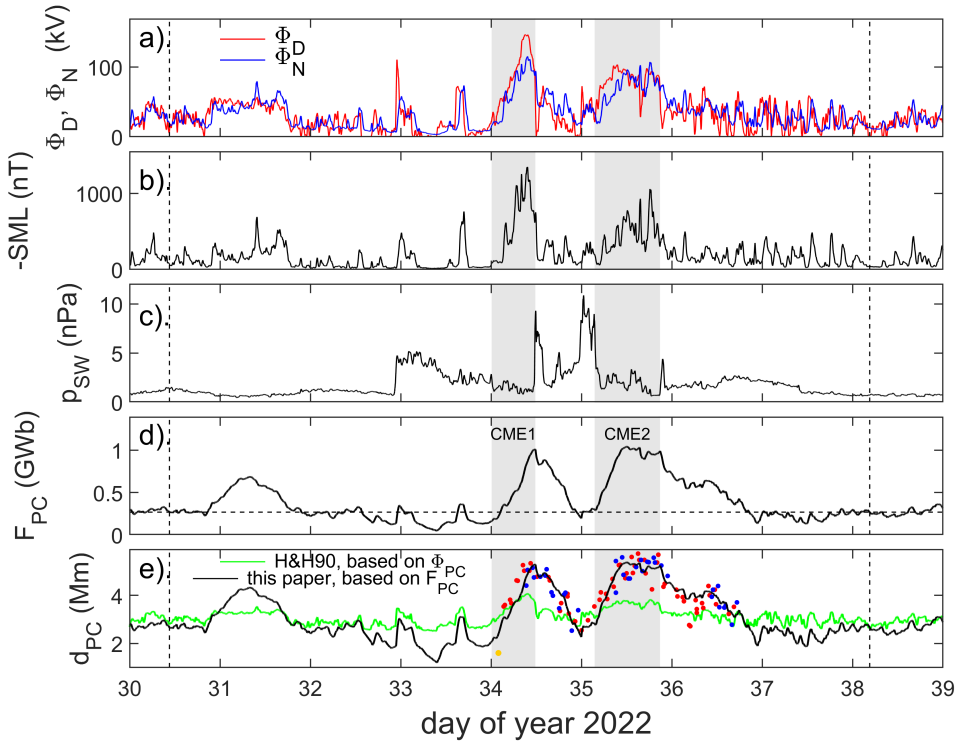

Figure 6. Modelled variations of polar cap voltages, flux and diameter. The vertical dashed lines delineate the "calibration interval" defined in the text. (a) the dayside magnetopause reconnection voltage (Φ_D, in red) and the nightside tail current sheet voltage (Φ_N, in blue). (b). *-SML* (c). the solar wind dynamic pressure, p_{SW} (d). The open polar cap flux, F_{PC}. (e). The polar cap diameter d_{PC} (black line) derived from F_{PC} using interpolation of the variation defined by Equation 3 and (green line) derived from Φ_{PC} using the fit presented by Hairston and Heelis (1990) (H&H90). The modelling uses $\tau_N = 6.81min$ (see text for details). The red and blue dots show dawn-dusk polar cap diameters taken from images by the Special Sensor Ultraviolet Spectrographic Imagers (SSUSI) instruments on board the Defense Meteorological Satellite Program (DMSP) F-17 and F-18 satellites. (see Figure 7),

Figure 5a gives the predicted dayside reconnection voltage Φ_D computed from the interplanetary measurements: the other panels give the normalised variations of the terms from which it is computed. It can be seen that the mass density in each CME was slightly depressed and the transverse component of the IMF was enhanced, particularly during the first CME. The solar wind speed factor varied by about ±10% in the interval: it was increased by the passage of CME1 but fell during CME2 and rose again roughly 12 hours after it had passed. Figure 5d shows that the IMF swings to strongly southward towards the end of the first CME passage and during much of the second CME passage, giving higher Φ_D at these times. The first CME gives a particularly large peak in Φ_D near its trailing edge, reaching $150kV$ and exceeding $85kV$ for $5.7hr$ (6.1 to 11.8 hr UT on d-o-y 34). The second CME gives are more sustained period of somewhat smaller magnetopause reconnection voltage, being between $85kV$ and $103kV$ for most of an interval of duration $11.3hr$ (9.4 to 20.7 hr UT on d-o-y 35).

4 Analysis of polar cap behaviour during the event

Part (a) of Figure 6 shows the variation of Φ_D computed using Equation 5 in red. In blue is the estimated variation of Φ_N, computed from the observed *SML* index variation, shown in part (b), using Equations 6, 7 and 8. Part (d) shows the variation in open flux F_{PC} derived using equation 9. These variations use the optimum combination of $\tau_N = 6.81min$ and $k(F) = 0.9972$. It was found that $\tau_N \leq 5.33min$ gave times when F_{PC} became negative during the calibration interval and that $\tau_N \geq 10.52min$ gave times when F_{PC} exceeded $1.2GWb$, which is larger than the values reported in the literature and than a proposed upper limit for a saturated polar cap. Substorm onsets are typically initiated when F_{PC} reaches about $0.9GWb$ (Milan et al., 2008) but larger values, up to about $1.1GWb$, have been deduced in sawtooth events and steady convection events (DeJong et al., 2007; Lockwood et al., 2009; Brambles et al., 2013). It has been estimated that in large superstorms, F_{PC} effectively saturates at $1.2GWb$ (Mishin & Karavaev, 2017). In order to set the value of τ_N within this allowed range, we look at the modelled diameter of the polar cap in the calibration interval, as this a strong function of τ_N. The black line in Part (e) shows the variation in d_{PC} for the variation of F_{PC} shown in Part (d). This is obtained by PCHIP interpolation of the variation of F_{PC} with d_{PC} given by Equation 3. The green line in Figure 6d is from an empirical fit to DMSP ionospheric convection data given in Figure 5 of Hairston and Heelis (1990) (H&H90) which yields d_{PC} as a function of transpolar voltage Φ_{PC} and which is here evaluated from Φ_D, Φ_N and Φ_V, using Equation 2. It can be seen that the variation of the two estimates of d_{PC} have similarities, but that the empirical model shows less variation than the one derived here. The Figure 5 of H&H90 shows considerable scatter about the fitted line and so this difference is not unexpected. It is also worth noting that the average variation deduced from that plot is quite similar to the variation derived theoretically by Siscoe (1982). The value of $\tau_N = 6.81min$ adopted here makes the averages of these two variations the same over the calibration interval. It yields an open flux $F_{PC} = 0.26GWb$ at the start and end of the calibration interval, which is lower than the average value near $0.4GWb$ in the surveys by Boakes et al. (2009) and Milan et al. (2021). It also yields peak values of $1.01GWb$ at the end of CME1 and $1.03GW$ at the end of CME2. Valuable confirmation of the value of τ_N comes from images of the northern and southern auroral ovals by the Special Sensor Ultraviolet Spectrographic Imager (SSUSI) on board the Defense Meteorological Satellite Program (DMSP) F-17 and F-18 satellites (Paxton et al., 2002, 2021). These images are in the the Lyman-Birge Hopfield (LBH) short band (LBHS, 140–160 nm) of molecular nitrogen and the observed swathes usually show the full extent dawn-dusk diameter of the dark region poleward of the auroral oval. The poleward edge of the aurora seen in Far Ultraviolet (FUV) is often used as a proxy indicator of the OCB (Longden et al., 2010) and the six DMSP/SSUSU FUV images presented in Figure 2 of Y. Zhang et al. (2022) for the period studied here indicate considerable variability of the polar cap diameter.

In general, there is a difference between the latitude of the OCB, as identified in particle precipitation data and the poleward edge of the aurora, giving a dark ring of closed field lines poleward of the poleward edge of the aurora. The latitudinal width of this offset, $\delta\Lambda$ will, to some extent, depend on the imager, the magnetic local time (MLT) and the intensity of the auroral precipitation. Carbary et al. (2003) found that $\delta\Lambda$ did vary systematically with MLT but argued a constant value of 3.5° could be used for the purposes of computing F_{PC}. Boakes et al. (2008) found $\delta\Lambda \leq 1°$, except in the predawn and evening sectors, where values up to 2° may apply. Longden et al. (2010) find that near dawn and dusk, the sectors of interest here, $\delta\Lambda \approx 1°$ applies and that is what we adopt here.

There is an interesting minimum in the modelled F_{PC} at UT of $9.5hrs$ on d-o-y 33 which is as low as $0.05GWb$. This followed an interval of duration $4hr$ of strongly northward IMF when Φ_D was essentially zero. This is slightly lower than the lowest re-

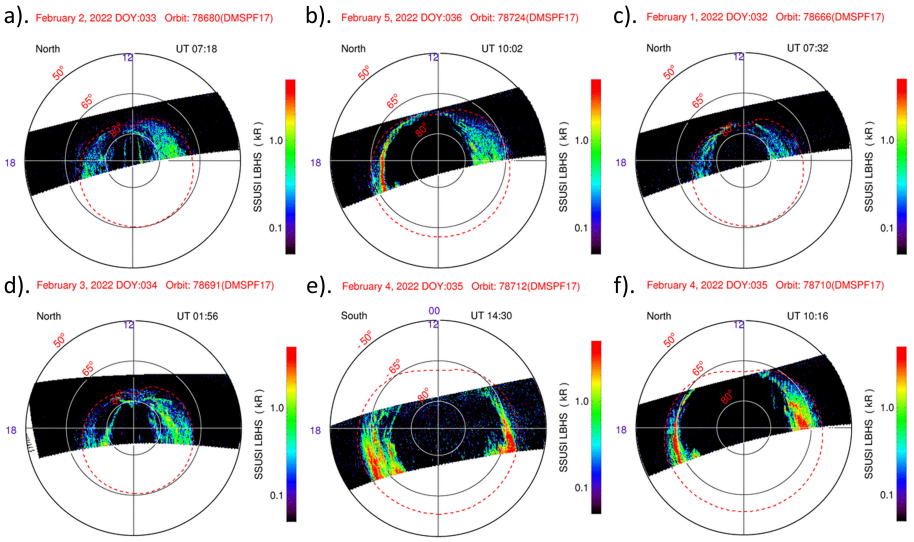

Figure 7. Selected sample auroral images recorded by the Special Sensor Ultraviolet Spectrographic Imagers (SSUSI) instruments on board the Defense Meteorological Satellite Program (DMSP) F-17 and F-18 satellites in the Lyman-Birge Hopfield (LBH) short wavelength band (LBHS, 140–160 nm). See text for details.

ported F_{PC} that we know of in the literature ($0.08GWb$), which may indicate our value for τ_N is slightly too low. Nevertheless, the τ_N used in Figure 6 does give a range of F_{PC} values that matches distribution previously reported in the literature. It is worth noting that panel (c) of Figure 6 shows that the solar wind dynamic pressure, p_{SW} is raised above previous levels at this time and, as mentioned above, this could have enhanced Φ_{N2}, reducing F_{PC} values.

Figure 6e gives the modelled dawn-dusk polar cap diameter d_{PC} predicted using the assumption that the polar cap remains circular. We here used the dawn-dusk diameter deduced from DMSP/SSUSI images only as a rough check on that modelling. A major reason it can be of no greater significance than this is that, in reality, the polar cap is far from circular at some times. This is illustrated by Part (a) of Figure 7. This shows the aurora as seen by the F-17 satellite during a pass over the quiet, contracted polar cap in the northern hemisphere at 07:18 UT on d-o-y 33: this is during the descent towards the deep minimum in F_{PC} at $UT = 9.5hrs$ noted above. This pass reveals a horse-collar aurora with the putative OCB marked by narrow arcs that are almost parallel to the noon-midnight meridian (Wang et al., 2022). The polar cap is very far from circular at this time. Figure 7d shows a later pass at $01:56UT$ on d-o-y 33, close to the time of the arrival of the first CME. The horse-collar form is still present and the dawn-dusk dimension of the dark polar cap gives a value of d_{PC} that is shown by the orange point in Figure 7e: this is lower than the value predicted for a circular polar cap because of the horse-collar form is still present to some degree. In general, polar caps becomes more circular as the open flux increases. The other panels of Figure 7 give examples. Parts (c), (b) and (f) are northern hemisphere passes for, respectively, small, moderate and large open flux, in which the visible part of the polar cap, at least, is more circular in form. Part (e) is an example of a southern hemisphere pass of F-17 over a relatively large polar cap. Southern hemisphere passes of both F-17 and F-18 tend to be toward the nightside. We use passes where the poleward edge of the aurora is detectable within 1 hr of the dawn-dusk MLT meridian and extrapolate the poleward boundary over up to 1 hr

of MLT if it does actually cross the meridian in the observed swathe. We apply $\delta\Lambda$ of 1° at both 18 and 06 MLT. The results are shown for pases of F-17 and F-18 over the northern and southern hemisphere polar caps by, respectively, red and blue points in Figure 7e. Cases where the polar cap is far from circular, such as in parts (a) and (d) are not used. The results show considerable scatter which is readily explained by the changes in shape of the polar cap, but do reveal the polar cap expansion and contraction during and after the CME impacts. They also provide confirmation that the value for τ_N used is appropriate.

The variations in the nightside voltage Φ_N and the polar cap flux F_{PC} in Figure 6 follow that in the magnetopause voltage Φ_D in ways that we would expect. Towards the end of d-o-y 30 there is a sharp rise in Φ_D that is followed by a similar, but smaller, rise in Φ_N. The high Φ_D persists for almost a day, declining only slightly. The mismatches in these voltages causes the polar cap flux F_{PC} to rise to a peak of $0.68GWb$ at 8.4 UT of d-o-y 31 and then fall back to its initial value near $0.26GWb$. This day-long event appears to be a period of driven convection and there is a slight rise in -*SML* related nightside reconnection Φ_{N1} at its end. The next interesting feature is a sharp spike in Φ_D just before the end of d-o-y 32. This generates a response in -*SML* and hence Φ_{N1} and the rise in F_{PC} is small and short-lived. This appears to be a small isolated substorm cycle in which -*SML* does not rise above $478nT$. The decay in F_{PC} to the deep minimum discussed above occurs after this event: we see Φ_D and *SML* fall to essentially zero for almost a day and the exponential decay of open flux due to Φ_{N2} can clearly be seen. After this, a second, stronger isolated substorm cycle occurs in which -*SML* rises to $763nT$ but, again, the rise in F_{PC} is small and short-lived.

It is after this that CME1 arrives. Φ_D ramps up considerably, as does -*SML* and Φ_{N1} but with a lag and by a smaller degree so the open flux grows to a peak of $1.01GWb$. The *SML* index shows a series of spikes that suggest substorms, but Φ_D is large and keeps increasing, causing it to always exceed Φ_N and so F_{PC} keeps rising. Only after the CME has passed and Φ_D declines sharply does Φ_N dominate and reduce the open flux. This rapid decline is caused by the loss rate Φ_{N1} but between enhancements in -*SML* we see that Φ_{N2} also contributes. Again we note that in this interval between CME1 and CME2 Figure 6c shows considerably enhanced p_{SW} and this may have contributed to the decline in F_{PC} by enhancing Φ_{N2}.

CME 2 is somewhat different. The rises in Φ_D, Φ_N and -*SML* are more modest than in CME1. Again spikes in *SML* suggest a series of substorms. For this second event, the response in Φ_N, is slower and so F_{PC} grows to levels that slightly exceed those attained in CME1 ($1.04GWb$), even though the driving voltage Φ_D is not as large in this second event. Towards the end of the passage of CME2, Φ_D and Φ_N are approximately balanced and the peak open flux is maintained. After the passage of CME2, intermittent Φ_D means that the decline in F_{PC} takes considerably longer and -*SML* remains low so the slow decline in F_{PC} is associated with Φ_{N2} more than Φ_{N1}.

It is useful to look at the relative contributions of the two open flux loss rates Φ_{N1} and Φ_{N2}. Figure 8 looks at the relationship of the two. Comparison of Parts (a) and (d) of Figure 8 shows that, in general, Φ_{N1} is greater than Φ_{N2}. Both increase with increasing transpolar voltage Φ_{PC} and hence the sum of the two does the same (Figure 8b). Part (e) shows the ratio of the two, Φ_{N1}/Φ_{N2}, as a function of Φ_{PC}, the mauve line is unity for this ratio and so Φ_{N1} always dominates for $\Phi_{PC}{\geq}85kV$. Figure 8f is the same ratio as a function of -*SML* and shows that Φ_{N1} always dominates for $-SML{\geq}27nT$; however, the plot also shows great variability in this ratio which is the effect of the amount of open flux F_{PC} on Φ_{N2}. This is also seen in Figure 8c which plots the total loss rate as a function of -*SML*. This reveals the form of Φ_{N1} given by Equation 6, but that Φ_{N2} has indeed added scatter; however, the scatter in Figure 8c is not as great as in Figure 3 because it is for 7 days of 1-minute data whereas Figure 3 is for 25 years of hourly data.

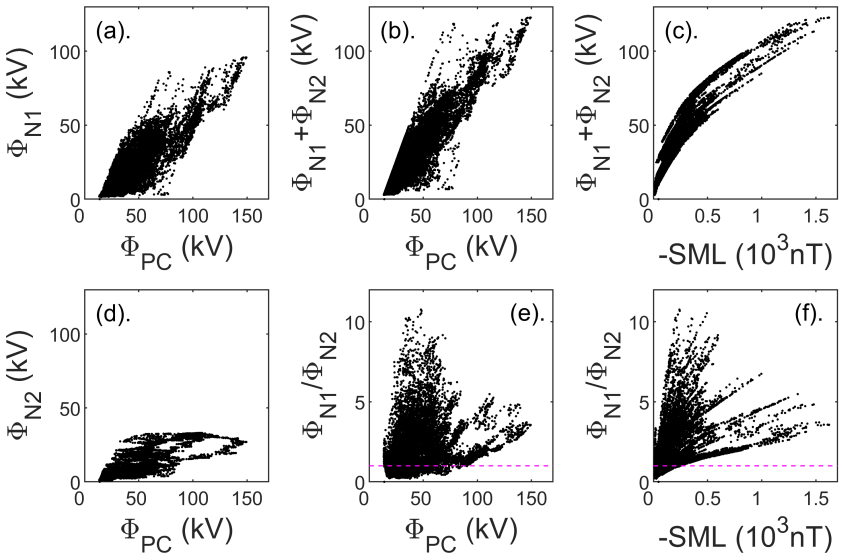

Figure 8. Scatter plots comparing the open flux loss rates associated with the nightside auroral electrojet,Φ_{N1}, and that associated with enhanced tail magnetic flux but without a signature in enhanced auroral electrojet activity, Φ_{N2}. Parts (a), (d), (b) and (e) show, as a function of transpolar voltage Φ_{PC}: (a) Φ_{N1}; (d) Φ_{N2}; (b) the total loss rate, $\Phi_N = \Phi_{N1} + \Phi_{N1}$, and (e) the ratio of the two, Φ_{N1}/Φ_{N2}. (c) and (f) show, respectively, the sum and the ratio of the two loss voltages as a function of the *-SML* value. Data are for the "calibration interval" between the two vertical dashed lines in Figure 6. Mauve dashed lines in parts (e) and (f) show where the two loss rates are equal.

We conclude that the loss rate of open flux is largely dependent on the *SML* auroral electrojet index and although the loss Φ_{N2} that is not captured by *SML* is relatively small, it is still important for the application of the ECPC model because otherwise estimated open fluxes rise to levels that are not seen in the real magnetosphere.

It is interesting to note that Figure 6d shows that the open flux F_{PC} between the CMEs fell to $0.20GWb$, just below the value at the start and end of the calibration interval. This eliminates preconditioning effects of CME1 on the response to CME2, at least in terms of residual open flux. In this context, we also note that 4c shows that the ring current indices *-SMR* and *-SYM-H* fell back down after CME1 to only just above their values before the arrival of CME1. (Their decay after CME2 was noticeably slower). This seems to argue against major preconditioning in terms of ring current energy as well. There are other possible pre-conditioning effects such as the thickness of the plasma sheet and the speeds of polar thermospheric winds. The latter, however, would tend to reduce the heating effect of CME2 not increase it.

5 The Effect of Earth's eccentric magnetic field

The previous section shows that the polar cap expanded and contracted during the events in early February 2022. In this section we add to the effects of this the UT variations caused by the diurnal rotation of Earth's eccentric magnetic field. The motions are computed using the eccentric dipole model of the geomagnetic field by Koochak and Fraser-Smith (2017), as discussed by Lockwood et al. (2021).

Figure 9 demonstrates the effect of polar cap motions. Panel (a) shows the transpolar voltage Φ_{PC} computed using Equation 2 from the variations of Φ_D and Φ_N (with constant Φ_V) derived in the previous section. Part (b) shows the dawn-dusk voltages induced in the north and south polar cap, in a geocentric frame, by the diurnal cycle of sunward/antisunward polar cap motion, respectively ϕ_{MN} and ϕ_{MS}. Note that for constant dawn-dusk polar cap diameter, these would be sine waves and the dashed lines give the variation for the mean of the polar cap diameter over the calibration interval τ, $\langle d_{PC} \rangle_\tau = 3.08Mm$ (roughly equivalent to a latitudinal polar cap angular radius of 13°). Note also that the amplitude of the sine wave is smaller for the northern hemisphere because the offset of the rotational and magnetic pole is smaller in the north and that the sine waves are not in antiphase because for the eccentric dipole field model used the magnetic poles are not 180° apart in longitude (as they would be for a geocentric dipole).

Figure 9c shows the average transpolar voltage allowing for the motions of both polar caps, computed using Equations 10 and 11 for the northern and southern hemisphere, Φ'_{NC} and Φ'_{SC} shown in red and blue, respectively. The black line is the average of the two, Φ'_{PC} which is different from the transpolar voltage in the absence pole motions Φ_{PC}, which is shown in Figure 9a and by the grey area in Figure 9c. If Φ' in a hemisphere is smaller than Φ_{PC} it means that polar cap is moving towards the Sun. Let us apply Faraday's law to a loop PCGS, fixed in a geocentric frame, where P and C are the dawn and dusk flanks of the ionospheric polar cap which map along open geomagnetic field lines to the points G and S, respectively, just outside the bow shock in interplanetary space, often referred to as the "Stern Gap", SG (see Lockwood & Cowley, 2022). The antisunward flow of the solar wind, with frozen-in open magnetic field, between S and G adds to the magnetic flux threading the loop PCGS and the sunward convection of frozen-in field in the F-region ionosphere between P and C removes flux from that loop. Hence if sunward polar cap bulk motion is slowing the rate that magnetic flux is transferred antisunward across PC in the ionosphere, it is reducing the rate at which flux removed from the loop. Hence this situation means that less energy is being directly deposited in the ionosphere but more magnetic energy is being stored in that hemisphere of the tail lobe. Conversely, If Φ' exceeds Φ_{PC}, the polar cap is moving away

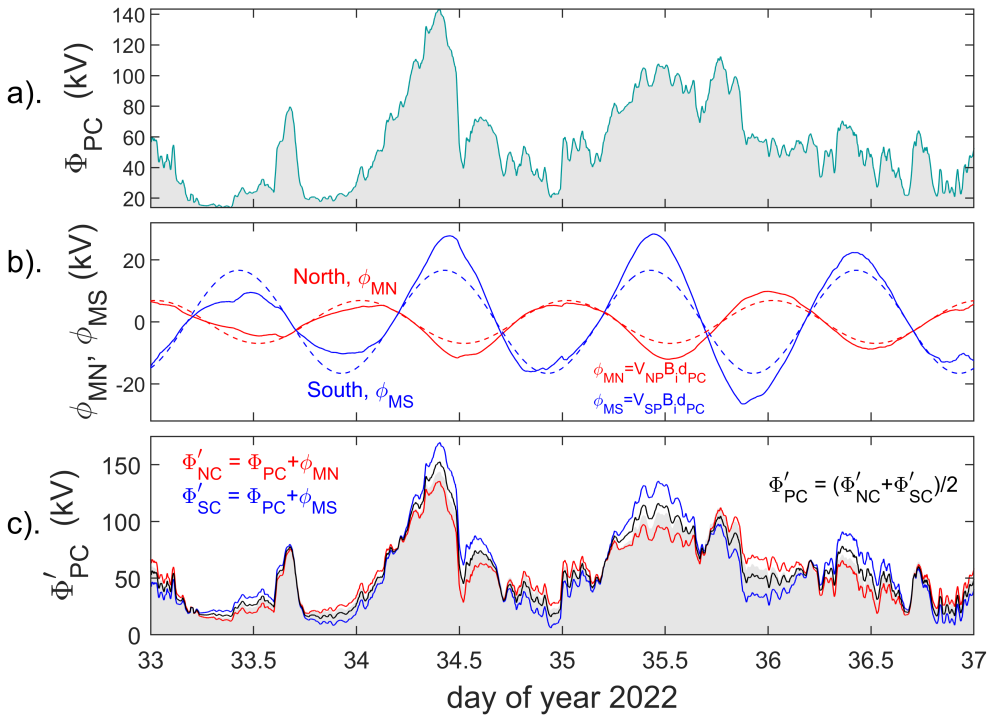

Figure 9. Analysis of the effect of pole motions on transpolar voltage during the events of early February, 2022. (a). The transpolar voltage derived from Equation 2, Φ_{PC}. (b). The voltages across the northern (ϕ_N, in red) and southern (ϕ_S, in blue) polar caps in a geocentric reference frame (such as GSM or GSE) induced by the diurnal motions of the poles (see Equations 10 and 11). Note that these variations would be sinusoidal if the polar cap diameter d_{PC} were constant (see Lockwood et al., 2021) but here depart from sine waves because we apply the modelled variations in d_{PC} shown in Figure 6d. The dashed lines are the variations for the mean value of the polar cap diameter over the calibration interval τ, $\langle d_{PC} \rangle_\tau = 3.08 Mm$. (c). The variations in voltages in the GSE/GSM frames allowing for pole motions in the northern hemisphere, Φ'_{NC} (in red) and in the southern hemisphere, Φ'_{SC} (in blue). The black line is the average of the two (Φ'_{PC}) and the grey area gives the uncorrected voltage, Φ_{PC}, repeated from panel (a) to aid comparison.

from the Sun (i.e. with the solar wind) so that more energy is being directly deposited in ionosphere but less energy is being stored in that hemisphere of the tail lobe.

It is worth noting that some of these diurnal cycles may have been missed in some magnetometer observations of geomagnetic activity as they were attributed to the Sq variation. This is because to reveal geomagnetic activity, magnetometer data usually has subtracted from it a quiet diurnal variation to remove the effects of dynamo action, of particular, solar thermal tides and the equatorial electrojet that give the Sq variation (Yamazaki & Maute, 2017). The polar cap diameter d_{PC} will be small in quiet times but not zero and so the pole motions effect may have added to the quiet day diurnal variation that is subtracted. This is most likely to be the case inside the polar cap and so a factor for the Polar Cap Indices (PCI). We searched for an effect of the different polar motions during this event in the published provisional Northern and Southern hemisphere PCI. Their variations are both very similar to the *-SML* index and so appear to be dominated by the auroral electrojet in this event. We note that some other studies have almost certainly detected signatures of the pole-motion effect but have generally attributed it to ionospheric conductivity effects.

6 The Importance of the Universal Time of CME arrival

Owens et al. (2020) has discussed the value of accurate prediction of the arrival time of CME impacts on Earth's magnetosphere. They make the point that if false-alarms are a serious problem, accurate arrival time information is only valuable if the geoeffectiveness of the CME can also be forecast. The analysis presented in this paper adds a further complication to that discussion in that the geoeffectiveness of a CME is shown to depend upon the Universal Time of the CME arrival.

To investigate the effect of pole motions in isolation, we here consider that the voltages Φ_D and Φ_N would not depend on the Universal Time of the CME impact. The phase of the diurnal cycles of pole motions have an influence on geoeffectiveness through the modification of Φ_{PC} to Φ'_{NC}, Φ'_{SC} and Φ'_{PC}.

However, in reality, the dipole tilt (and hence Universal Time) will influence Φ_D through its effect on the magnetic shear at, and length of, the magnetopause reconnection X-line via the Russell-McPherron (R-M) effect (Russell & McPherron, 1973; Lockwood, Owens, Barnard, Haines, et al., 2020). In our synthesis of the effects of a delayed arrival of a CME, we allow for this by lagging (by a delay δt) the variations in the factors $B_\perp$, ρ_{sw}, and V_{sw} in Equation 5; however, the term $sin^d(\theta/2)$ cannot be simply lagged in the same way. The reason is that the clock angle θ is computed in the GSM frame and because of the UT variation in the rotation angle γ between the GSE and GSM frames (caused by the dipole tilt variation with UT), the lagged values of IMF in the GSE frame, $[B_Z]_{GSE}$ and $[B_Y]_{GSE}$, have to be transformed for the γ of the new UT into $[B_Z]_{GSM}$ and $[B_Y]_{GSM}$ that are then used to compute $\theta = tan^{-1}(|[B_Y]_{GSM}|/[B_Z]_{GSM})$ and hence $sin^d(\theta/2)$ and Φ_D for the delayed arrival at Earth.

In general, there will probably also be UT effects on Φ_N. A number of papers have discussed mechanisms by which the dipole tilt can influence tail structure and dynamics and so introduce UT effects into reconnection responses in the tail (Kivelson & Hughes, 1990; Danilov et al., 2013; Kubyshkina et al., 2015; Lockwood, Owens, Barnard, Watt, et al., 2020; Lockwood et al., 2021). However as these effects are less well established than the R-M effect, we here simplify by investigating the effect of dipole tilts on Φ_D only. We do this by assuming the form of the temporal variation in Φ_N response is the same as for the unlagged $\delta t = 0$ case, as shown in Figure 6. This allows us to simply lag the Φ_N variation by δt. We then scale these lagged values of Φ_N so that the integral over the calibration interval (which is also lagged by δt) is equal to that of the recalculated, lagged Φ_D. This gives us the revised variation of Φ_{PC} for the δt considered, from Equa-

tion 2. We can study the R-M effect in isolation from this Φ_{PC} variation but also transform it into Φ'_{PC} (by evaluating Φ'_{NC} and Φ'_{SC} and averaging them) to study the combined effect of the R-M effect and the pole motions.

Figure 10a shows four variations associated with the CME events. These are: (1) the observed *SYM-H* geomagnetic index (in mauve); (2) the power deposited globally in the ionosphere and thermosphere by Joule heating, P_i, as modelled by Dang et al. (2022) (in green); (3) the square of the voltage derived here from the ECPC model but not allowing for polar cap motions Φ^2_{PC} (in orange); and (4) the square of the transpolar voltage derived here when polar cap motions are included $[\Phi'_{PC}]^2$ (in black). All four variations have been normalised to the large peak that occurred towards the end of CME1 and all are for no introduced synthetic lag (i.e., $\delta t = 0$). The power input predicted by Dang et al., P_i, has been lagged by $0.6hrs$ in this plot to give optimum agreement, we presume this accounts for propagation and response lags. We can see that, with this lag, P_i agrees very well with the variations in Φ^2_{PC} and $[\Phi'_{PC}]^2$ predicted here. P_i was derived from the observed solar wind and IMF parameters using the statistical convection model of Weimer (2005). If we use a simple resistor analogy the power deposited is proportional to the square of the voltage and so the square of the transpolar voltage is a simple proxy metric of Joule heating rate and indeed Robinson and Zanetti (2021) do find a good statistical square-law relationship between the two for the 27 geomagnetic storm events that they studied (see their Figure 2d). Hence the use of a steady-state convection model, driven by the upstream solar wind and IMF, yields a very similar global heating variation to that inferred here using the ECPC model. Note that *SYM-H* is of relevance to magnetospheric energetics being related to the energy content of the ring current; however, that relationship is not a straightforward one (Sandhu et al., 2021; Robinson & Zanetti, 2021). Of interest in the time series studied here is the fact that peaks in Joule heating of the ionosphere after each CME are associated with the time of enhanced auroral activity as identified by the bursts of enhanced *-SML* and enhanced Φ_N. However, a lower level of Joule heating does continue after *-SML* declines when *SYM-H* remains enhanced and the polar cap flux F_{PC} is decaying slowly. This appears to be due to the "quiet" open flux loss that is not associated with *SML* and energy stored in the tail lobes is quietly (without auroral electrojet activity) deposited in both the ionosphere and ring current.

Figure 10a shows that the proxy for global heating rate from our analysis $[\Phi'_{PC}]^2$ is similar to the results of the steady-state model of Weimer (2005). However, Figure 10b shows there is a major difference. The Weimer model predicts the same transpolar voltage in the two polar caps and only some dipole tilt effects on conductivity would give any difference in Joule heating between the two hemispheres. We here predict that both the transpolar voltage and the Joule heating have strong Universal Time variations that are close to being in antiphase in the two polar caps. The precise behaviour depends on the Universal Time of the storm-time rise in Φ_D and that is one reason why CME1 and CME2 have such different effects in these events. Figure 10b shows that during CME1 the two hemispheres show similar temporal variations in $[\Phi'_{NC}]^2$ and $[\Phi'_{SC}]^2$ but the southern hemisphere value is considerably larger. During CME2, $[\Phi'_{SC}]^2$ again dominates initially but for the peak at the end of the passage of CME2 the Joule heating is dominated by $[\Phi'_{NC}]^2$. Therefore, although the two methods predict very similar global Joule heating power, the temporal variation of the deposition into the two polar caps is more complex in our analysis. The behaviour during CME2 is more complex than for CME1 because, in addition to the pole motions, the Φ_N rise is delayed after the causal rise in Φ_D (see Figure 6a).

The bottom panel of Figure 10 shows the combined effect of introducing synthetic lags δt in arrival time at Earth in the range [0:2:12] hrs, via both the R-M and pole-motion effects. It shows the $[\Phi'_{PC}]^2$ variations for each value of δt, derived as described above.

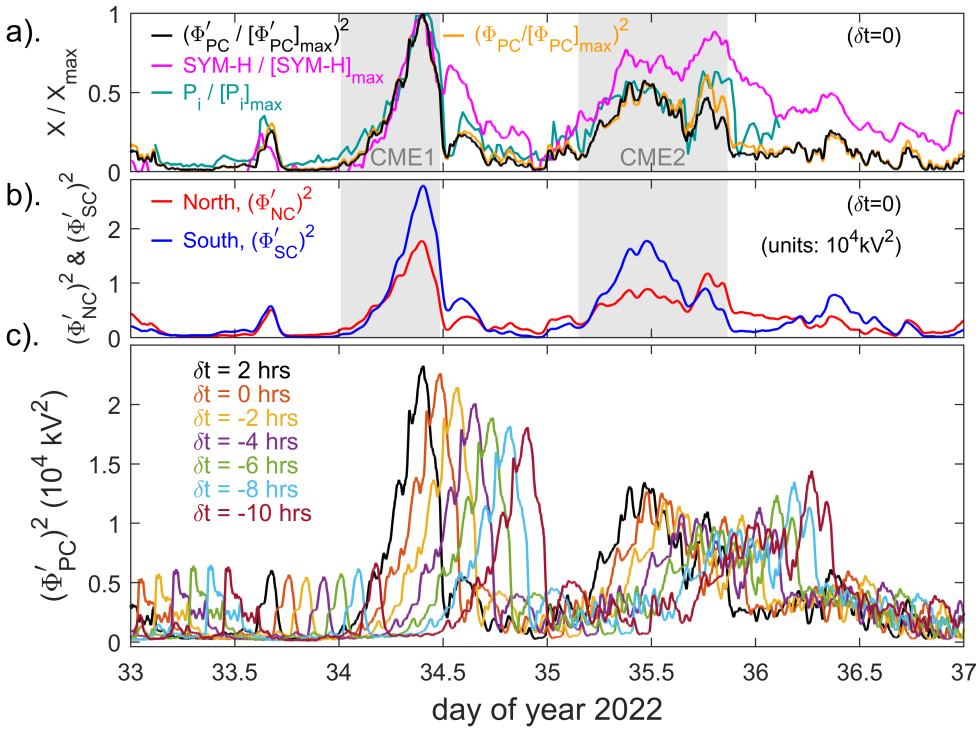

Figure 10. Analysis of the effects of CME arrival time. (a) shows (in mauve) the variation of the *SYM-H* geomagnetic index; (in green) the power deposited in the auroral ionospheres, P_i, as modelled for these events by (Dang et al., 2022); (in orange) the square of the transpolar voltage neglecting pole motions, as shown in green in Figure 9a, Φ^2_{PC}; and (in black) the square of the average polar voltage with pole motions, as shown in black in Figure 9c, $[\Phi'_{PC}]^2$. All four are normalised by their peak value towards the end of the passage of CME1 and all three are shown in the panel without any synthetic lag δt being introduced other than for P_i which has been lagged by 0.6hrs. (b). shows the variations of the square of the transpolar voltages in the northern and southern polar caps allowing for pole motions, $[\Phi'_{NC}]^2$ and $[\Phi'_{SC}]^2$, respectively. In (c) the interplanetary data sequences are lagged by δt but the IMF orientation factor in GSM recomputed for the different UT of arrival in evaluating Φ_D (the Russell-McPherron effect, R-M) as well as the different phase of the diurnal cycles of pole motions (the pole motion effect). The response of the nightside reconnection voltage Φ_N is assumed to be the same in waveform (but lagged by δt) as that for $\delta t = 0$ but is scaled such that the integral over the calibration interval matches the integrated revised Φ_D. For each lag (Φ'_{NC}) and (Φ'_{SC}) are computed. The plot shows the square of the average of the two, $[\Phi'_{PC}]^2$ as a function of time for δt which is varied between 0 (black line, as also shown in part a) and $12 hrs$ (blue line).

Figure 10c demonstrates that the peak $[\Phi'_{PC}]^2$ at the end of CME1 would have been considerably smaller if the event had arrived some hours later. Figure 11 analyses the relative contribution of the R-M effects and the pole motions to the combined variation with arrival time shifts δt between -12 hrs and +12 hrs (δt = [-12:0.1:12]hrs). The event is here taken to be between the start of d-o-y 34 and d-o-y 36.5 (in unshifted time) which runs from the start of CME1, to near the end of the recovery from CME2. Figure 10a shows that $[\Phi'_{PC}]^2$ is a plausible approximate proxy for the global Joule heating rate and the maximum and event-integrated values are computed for each value of δt. Part (a) shows the variations for the peak $[\Phi'_{PC}]^2$ which occurs at the end of CME1. Part (b) shows the integral of $[\Phi'_{PC}]^2$ over the event interval, as defined above. It can be seen in Part (a) that the R-M effect (in mauve) is relatively minor for the induced UT changes in the peak power deposited, the total variation (in black) of the peak being dominated the pole-motion effect (in green). In this case, the R-M effect causes the opposite effect on the peak to the pole motion: this is not a general result, for example, the R-M effect would be reversed if the IMF $[B_Y]_{GSE}$ had the opposite polarity. Hence the two effects tend to cancel in this case, but because the pole-motion effect is larger the net effect is still considerable. However for the integrated power deposited by the two CMEs, shown in Part (b), the variations caused by the two effects are more similar in amplitude and not so close to being in antiphase and the net effect is smaller but still present.

The combination of the two effects causes a variation in the peak $[\Phi'_{PC}]^2$ between 82.7% at $\delta t = 10.8hrs$ (and at $\delta t = -13.2hrs$) and 100.4% at $\delta t = 0.8hrs$ showing that the CME events arrived at almost the optimum UT for generating maximum heating effect in the thermosphere and that the peak would have been 17.3% smaller if the the event had arrived 13.2 hours earlier or 10.8 hours later. It should be noted that the R-M effect depends on the temporal variation of the IMF Y and Z components in GSE just before or after the peak (for $\delta t > 0$ and $\delta t < 0$, respectively, and so the R-M effect on the peak in other events could be considerably different. The integrated power over the event varies between 92.5% at $\delta t = -11.6hrs$ (and 12.4 hrs) and 100.05% at $\delta t = 0.2hrs$. This is a smaller effect than that on the peak value but still considerable.

It is interesting that the maximum in both curves is close to $\delta t = 0$, which shows that the thermospheric heating would have been smaller had the CMEs arrived at almost any other UT.

7 Discussion and Conclusions

The introduction to this paper gave the occurrence probability of events of the magnitude of the 3-4 February 2022 events in the *kp* and *am* geomagnetic index datasets that extend back to 1932 and 1959, respectively. We have near-continuous IMF (with continuous *SML* data) since 1995 and to compare with the geomagnetic data occurrence statistics it is important to use the subset of the index datasets over the same interval. The reason is that the decline in the open solar flux since 1985 has caused a similar long-term decline in geomagnetic activity (Lockwood et al., 2022). The *kp* and *am* indices after both the CME impacts in the events studied here peaked at 5+ and $84nT$, levels that have been detected or exceeded, for, respectively, 1.22% and 1.13% of the years 1995-2021, inclusive. The figure for the *am* index is the most significant because it has the most uniform response to solar wind forcing with time-of-year and Universal Time of all the geomagnetic indices because it employs the most uniform geographical network of stations, using two hemispheric rings of near-equispaced mid-latitude stations (Lockwood, Chambodut, et al., 2019).

It is interesting to compare with the *-SML* index which, in 10-minute running means, peaked at $1348nT$ and $1059nT$ after CME1 and CME2, respectively. These values have been detected or exceeded 0.07% and 0.23% of the interval 1995-2021. Similarly the 10-minute running means of the inferred dayside magnetopause reconnection voltage Φ_D

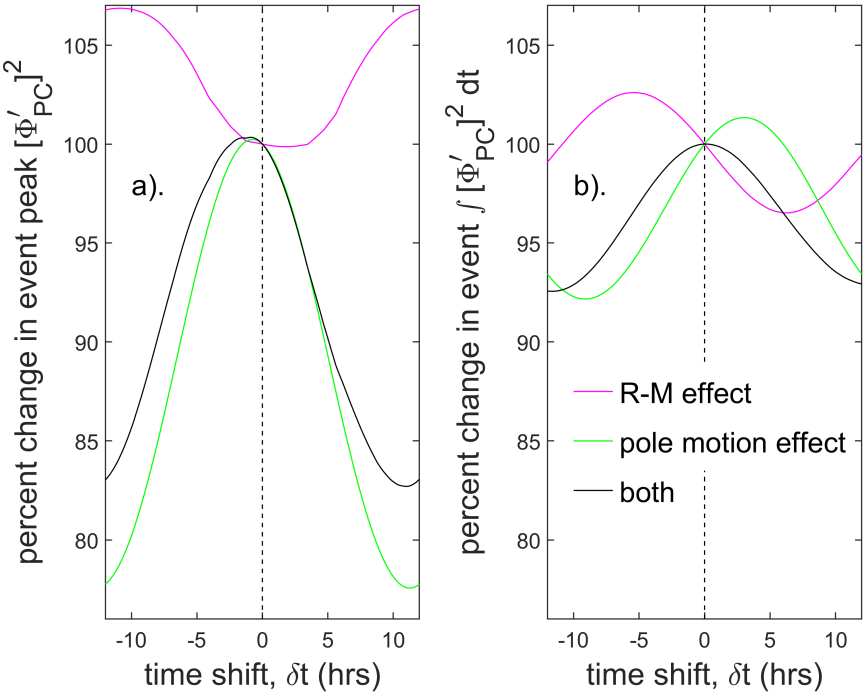

Figure 11. The computed effect of variation in the UT of arrival of the interplanetary disturbance on the $[\Phi'_{PC}]^2$ proxy for thermospheric Joule heating rate. The mauve lines show the effect of δt on $[\Phi'_{PC}]^2$ via the R-M effect and the green lines show the effect via the phase of the diurnal pole motions. The black lines show the combination of both effects. All three are shown as a function of the synthesised lag in the UT of the events' arrival, δt. (a) shows the variations in the amplitude of the large peak in $[\Phi'_{PC}]^2$ at the end of CME1 and (b) shows the variations for the integral of $[\Phi'_{PC}]^2$ over the lagged event (between decimal day of year $34 + \delta t/24$ and $36.5 + \delta t/24$, where δt is in hours).

peaked at $148.2kV$ and $103.7kV$ after CME1 and CME2, values that were found for 0.13% and 0.63% of the same interval. Hence the events were significantly more unusual and extreme in the -*SML* and Φ_D values than in the 3-hourly planetary indices.

We have here investigated the magnetospheric response to the two CMEs that impacted Earth on 3 and 4 February 2022 and famously led to the loss of many recently-launched Starlink satellites. Using statistical relationships to derive the variations in reconnection rate in the dayside magnetopause and in the cross-tail current sheet from the observed variations of interplanetary space and of the *SML* auroral electrojet index. We find that, in addition to a loss rate of magnetospheric open flux related to *SML*, that a smaller loss rate, not detected by *SML* but proportional to the open flux is needed to prevent unfeasibly large polar cap fluxes (below about 1 GWb). Using a loss rate time constant of $\tau_N = 6.8$min we match the polar cap diameters inferred from auroral images, making the simplifying assumption of a circular polar cap.

The dawn-dusk diameter of the open polar cap inferred in this way was than used to compute the voltage contributions made by the diurnal pattern of polar cap motions in a geocentric frame. We then use this, along with the well-understood Russell-McPheron effect on magnetopause voltage, to evaluate what the response would have been, and in particular a proxy for the Joule heating of the themosphere, if the CME's had arrived at different Universal Times.

We have shown that the CMEs in the events of early February 2022 arrived at close to the Universal Time which gave optimum heating of the thermosphere. This is particularly true for the peak of the heating burst at the end of the first CME, but is also true for the integrated heating over the duration of both CME events and their immediate aftermath. We show that the heating peak could have been lower by up to 17.3%, and the integrated heating lower by up to 7.5%, had the events arrived roughly 12 hours earlier or 12 hours later.

This adds another dimension to prediction of terrestrial space weather events: we have known for many years that we need to develop techniques to better predict the IMF field strength and orientation embedded in events, but we need to also predict the time-of arrival with some accuracy to make best use of that information and predict the geo-effectiveness of the event.

References

Anderson, B. J., Korth, H., Waters, C. L., Green, D. L., Merkin, V. G., Barnes, R. J., & Dyrud, L. P. (2014). Development of large-scale Birkeland currents determined from the Active Magnetosphere and Planetary Electrodynamics Response Experiment. *Geophysical Research Letters*, *41*(9), 3017–3025. Retrieved 2022-11-12, from http://doi.wiley.com/10.1002/2014GL059941 doi: 10.1002/2014GL059941

Atkinson, G. (1967). An approximate flow equation for geomagnetic flux tubes and its application to polar substorms. *Journal of Geophysical Research*, *72*(21), 5373–5382. Retrieved 2022-11-11, from http://doi.wiley.com/10.1029/JZ072i021p05373 doi: 10.1029/JZ072i021p05373

Atkinson, G. (1978). Energy flow and closure of current systems in the magnetosphere. *Journal of Geophysical Research*, *83*(A3), 1089–1103. Retrieved 2022-11-10, from http://doi.wiley.com/10.1029/JA083iA03p01089 doi: 10.1029/JA083iA03p01089

Baker, D. N., Pulkkinen, T. I., Hesse, M., & McPherron, R. L. (1997). A quantitative assessment of energy storage and release in the Earth's magnetotail. *Journal of Geophysical Research: Space Physics*, *102*(A4), 7159–7168. Retrieved 2022-11-12, from http://doi.wiley.com/10.1029/96JA03961 doi: 10.1029/96JA03961

Bartels, J. (1949). The standardized index Ks and the planetary index Kp. *IATME Bulletin*, *12b*, 97.

Bartels, J., Heck, N., & Johnston, H. (1939). The three-hour-range index measuring geomagnetic activity. *J. Geophys. Res*, *44*, 411–454. Retrieved from https://doi.org/10.1029/TE044i004p00411 doi: 10.1029/TE044i004p00411

Billett, D. D., Grocott, A., Wild, J. A., Walach, M.-T., & Kosch, M. J. (2018). Diurnal variations in global Joule heating morphology and magnitude due to neutral winds. *Journal of Geophysical Research: Space Physics*. Retrieved 2022-11-10, from http://doi.wiley.com/10.1002/2017JA025141 doi: 10.1002/2017JA025141

Blockx, C., Gérard, J.-C., Coumans, V., Hubert, B., & Meurant, M. (2009). Contributions of the driven process and the loading-unloading process during substorms: A study based on the IMAGE-SI12 imager. *Journal of Geophysical Research: Space Physics*, *114*(A2), n/a–n/a. Retrieved 2022-11-11, from http://doi.wiley.com/10.1029/2008JA013280 doi: 10.1029/2008JA013280

Boakes, P. D., Milan, S. E., Abel, G. A., Freeman, M. P., Chisham, G., & Hubert, B. (2009). A statistical study of the open magnetic flux content of the magnetosphere at the time of substorm onset. *Geophysical Research Letters*, *36*(4), L04105. Retrieved 2022-10-23, from http://doi.wiley.com/10.1029/2008GL037059 doi: 10.1029/2008GL037059

Boakes, P. D., Milan, S. E., Abel, G. A., Freeman, M. P., Chisham, G., Hubert, B., & Sotirelis, T. (2008). On the use of IMAGE FUV for estimating the latitude of the open/closed magnetic field line boundary in the ionosphere. *Annales Geophysicae*, *26*(9), 2759–2769. Retrieved 2022-11-01, from https://angeo.copernicus.org/articles/26/2759/2008/ doi: 10.5194/angeo-26-2759-2008

Borovsky, J. E., Lavraud, B., & Kuznetsova, M. M. (2009). Polar cap potential saturation, dayside reconnection, and changes to the magnetosphere. *Journal of Geophysical Research: Space Physics*, *114*(A3), n/a–n/a. Retrieved 2022-11-10, from http://doi.wiley.com/10.1029/2009JA014058 doi: 10.1029/2009JA014058

Boudouridis, A. (2005). Enhanced solar wind geoeffectiveness after a sudden increase in dynamic pressure during southward IMF orientation. *Journal of Geophysical Research*, *110*(A5), A05214. Retrieved 2022-11-11, from http://doi.wiley

.com/10.1029/2004JA010704 doi: 10.1029/2004JA010704

Bower, G. E., Milan, S. E., Paxton, L. J., & Anderson, B. J. (2022). Occurrence statistics of horse collar aurora. *Journal of Geophysical Research: Space Physics*, *127*(5), e2022JA030385. Retrieved from https://agupubs.onlinelibrary.wiley.com/doi/abs/10.1029/2022JA030385 doi: 10.1029/2022JA030385

Brambles, O. J., Lotko, W., Zhang, B., Oulette, J., Lyon, J., & Wiltberger, M. (2013). The effects of ionospheric outflow on ICME and SIR driven sawtooth events. *Journal of Geophysical Research: Space Physics*, *118*(10), 6026–6041. Retrieved 2022-10-28, from http://doi.wiley.com/10.1002/jgra.50522 doi: 10.1002/jgra.50522

Caan, M. N., McPherron, R. L., & Russell, C. T. (1973). Solar wind and substorm-related changes in the lobes of the geomagnetic tail. *Journal of Geophysical Research*, *78*(34), 8087–8096. Retrieved 2022-11-11, from http://doi.wiley.com/10.1029/JA078i034p08087 doi: 10.1029/JA078i034p08087

Cai, L., Aikio, A. T., & Nygrén, T. (2014, December). Solar wind effect on Joule heating in the high-latitude ionosphere. *Journal of Geophysical Research: Space Physics*, *119*(12). Retrieved 2022-11-20, from https://onlinelibrary.wiley.com/doi/abs/10.1002/2014JA020269 doi: 10.1002/2014JA020269

Carbary, J. F., Sotirelis, T., Newell, P., & Meng, C.-I. (2003). Auroral boundary correlations between UVI and DMSP. *Journal of Geophysical Research*, *108*(A1), 1018. Retrieved 2022-11-01, from http://doi.wiley.com/10.1029/2002JA009378 doi: 10.1029/2002JA009378

Carter, J. A., Milan, S. E., Paxton, L. J., Anderson, B. J., & Gjerloev, J. (2020). Height-integrated ionospheric conductances parameterized by interplanetary magnetic field and substorm phase. *Journal of Geophysical Research: Space Physics*, *125*(10). Retrieved 2022-11-10, from https://onlinelibrary.wiley.com/doi/10.1029/2020JA028121 doi: 10.1029/2020JA028121

Connor, H. K., Zesta, E., Ober, D. M., & Raeder, J. (2014). The relation between transpolar potential and reconnection rates during sudden enhancement of solar wind dynamic pressure: OpenGGCM-CTIM results. *Journal of Geophysical Research: Space Physics*, *119*(5), 3411-3429. Retrieved from https://agupubs.onlinelibrary.wiley.com/doi/abs/10.1002/2013JA019728 doi: 10.1002/2013JA019728

Cowley, S. W. H., & Lockwood, M. (1992). Excitation and decay of solar wind-driven flows in the magnetosphere-ionosphere system. *Annales Geophysicae*, *10*, 103–115. Retrieved 2022-08-18, from https://ui.adsabs.harvard.edu/abs/1992AnGeo..10..103C (ADS Bibcode: 1992AnGeo..10..103C)

Dang, T., Li, X., Luo, B., Li, R., Zhang, B., Pham, K., ... Wang, Y. (2022). Unveiling the space weather during the Starlink satellites destruction event on 4 February 2022. *Space Weather*, *20*(8). Retrieved 2022-10-23, from https://onlinelibrary.wiley.com/doi/10.1029/2022SW003152 doi: 10.1029/2022SW003152

Danilov, A. A., Krymskii, G. F., & Makarov, G. A. (2013). Geomagnetic activity as a reflection of processes in the magnetospheric tail: 1. The source of diurnal and semiannual variations in geomagnetic activity. *Geomagnetism and Aeronomy*, *53*(4), 441–447. Retrieved 2022-11-03, from http://link.springer.com/10.1134/S0016793213040051 doi: 10.1134/S0016793213040051

DeJong, A. D., Cai, X., Clauer, R. C., & Spann, J. F. (2007). Aurora and open magnetic flux during isolated substorms, sawteeth, and SMC events. *Annales Geophysicae*, *25*(8), 1865–1876. Retrieved 2022-10-28, from https://angeo.copernicus.org/articles/25/1865/2007/ doi: 10.5194/angeo-25-1865-2007

Elphinstone, R. D., Murphree, J. S., Hearn, D. J., Heikkila, W., Henderson, M. G., Cogger, L. L., & Sandahl, I. (1993). The auroral distribution and its mapping according to substorm phase. *Journal of Atmospheric and Terrestrial Physics*, *55*(14), 1741–1762. Retrieved 2022-10-23, from https://linkinghub.elsevier.com/retrieve/pii/002191699390142L doi: 10.1016/0021-9169(93)90142-L

Fang, T., Kubaryk, A., Goldstein, D., Li, Z., Fuller-Rowell, T., Millward, G., ... Babcock, E. (2022). Space weather evironment during the SpaceX Starlink satellite loss in February 2022. *Space Weather*. Retrieved 2022-11-05, from https://onlinelibrary.wiley.com/doi/10.1029/2022SW003193 doi: 10.1029/2022SW003193

Finch, I. D., & Lockwood, M. (2007). Solar wind-magnetosphere coupling functions on timescales of 1 day to 1 year. *Annales Geophysicae*, *25*(2), 495–506. Retrieved 2022-08-18, from https://angeo.copernicus.org/articles/25/495/2007/ doi: 10.5194/angeo-25-495-2007

Finch, I. D., Lockwood, M. L., & Rouillard, A. P. (2008). Effects of solar wind magnetosphere coupling recorded at different geomagnetic latitudes: Separation of directly-driven and storage/release systems. *Geophysical Research Letters*, *35*(21), L21105. Retrieved 2022-08-18, from http://doi.wiley.com/10.1029/2008GL035399 doi: 10.1029/2008GL035399

Förster, M., & Haaland, S. (2015). Interhemispheric differences in ionospheric convection: Cluster EDI observations revisited. *Journal of Geophysical Research: Space Physics*, *120*(7), 5805–5823. Retrieved 2022-10-23, from https://onlinelibrary.wiley.com/doi/10.1002/2014JA020774 doi: 10.1002/2014JA020774

Gjerloev, J. W. (2012). The SuperMAG data processing technique. *Journal of Geophysical Research: Space Physics*, *117*(A9), n/a–n/a. Retrieved 2022-11-06, from http://doi.wiley.com/10.1029/2012JA017683 doi: 10.1029/2012JA017683

Grocott, A., Cowley, S. W. H., Sigwarth, J. B., Watermann, J. F., & Yeoman, T. K. (2002). Excitation of twin-vortex flow in the nightside high-latitude ionosphere during an isolated substorm. *Annales Geophysicae*, *20*(10), 1577–1601. Retrieved 2022-10-25, from https://angeo.copernicus.org/articles/20/1577/2002/ doi: 10.5194/angeo-20-1577-2002

Hairston, M. R., & Heelis, R. A. (1990). Model of the high-latitude ionospheric convection pattern during southward interplanetary magnetic field using DE 2 data. *Journal of Geophysical Research*, *95*(A3), 2333. Retrieved 2022-10-23, from http://doi.wiley.com/10.1029/JA095iA03p02333 doi: 10.1029/JA095iA03p02333

Hajra, S., Dashora, N., & Ivan, J. S. (2022). On the sources, coupling and energetics during supersubstorms of the solar cycle 24. *Journal of Geophysical Research: Space Physics*, *127*(10). Retrieved 2022-11-12, from https://onlinelibrary.wiley.com/doi/10.1029/2022JA030604 doi: 10.1029/2022JA030604

Hapgood, M. A., Liu, H., & Lugaz, N. (2022). SpaceX—sailing close to the space weather? *Space Weather*, *20*(3). Retrieved 2022-11-05, from https://onlinelibrary.wiley.com/doi/10.1029/2022SW003074 doi: 10.1029/2022SW003074

Hapgood, M. A., & Lockwood, M. (1993). On the voltage and distance across the low latitude boundary layer. *Geophysical Research Letters*, *20*(2), 145–148. Retrieved 2022-08-18, from http://doi.wiley.com/10.1029/93GL00063 doi: 10.1029/93GL00063

Holzer, R. E., McPherron, R. L., & Hardy, D. A. (1986). A quantitative empirical model of the magnetospheric flux transfer process. *Journal of Geophysical Research*, *91*(A3), 3287. Retrieved 2022-11-07, from http://doi.wiley.com/10.1029/JA091iA03p03287 doi: 10.1029/JA091iA03p03287

Hones, E. W. J., Craven, J. D., Frank, L. A., Evans, D. S., & Newell, P. T. (1989). The horse-collar aurora: A frequent pattern of the aurora in quiet times. *Geophysical Research Letters*, *16*(1), 37-40. Retrieved from https://agupubs.onlinelibrary.wiley.com/doi/abs/10.1029/GL016i001p00037 doi: 10.1029/GL016i001p00037

Hubert, B., Blockx, C., Milan, S. E., & Cowley, S. W. H. (2009). Statistical properties of flux closure induced by solar wind dynamic pressure fronts. *Journal of Geophysical Research: Space Physics*, *114*(A7), n/a–n/a. Retrieved 2022-11-11, from http://doi.wiley.com/10.1029/2008JA013813 doi: 10.1029/2008JA013813

Imber, S. M., Milan, S. E., & Hubert, B. (2006). The auroral and ionospheric flow signatures of dual lobe reconnection. *Annales Geophysicae*, *24*(11), 3115–3129. Retrieved 2022-10-23, from https://angeo.copernicus.org/articles/24/3115/2006/ doi: 10.5194/angeo-24-3115-2006

Kabin, K., Rankin, R., Rostoker, G., Marchand, R., Rae, I. J., Ridley, A. J., ... L., D. D. (2004). Open-closed field line boundary position: A parametric study using an MHD model. *Journal of Geophysical Research*, *109*(A5), A05222. Retrieved 2022-10-27, from http://doi.wiley.com/10.1029/2003JA010168 doi: 10.1029/2003JA010168

Kalafatoglu, E. E. C., Kaymaz, Z., Frissell, N. A., Ruohoniemi, J. M., & Rastätter, L. (2018). Investigating upper atmospheric joule heating using cross-combination of data for two moderate substorm cases. *Space Weather*, *16*(8), 987–1012. Retrieved 2022-11-20, from https://onlinelibrary.wiley.com/doi/10.1029/2018SW001956 doi: 10.1029/2018SW001956

Karlsson, S. B. P., Opgenoorth, H. J., Eglitis, P., Kauristie, K., Syrjäsuo, M., Pulkkinen, T., ... Romanov, S. (2000). Solar wind control of magnetospheric energy content: Substorm quenching and multiple onsets. *Journal of Geophysical Research: Space Physics*, *105*(A3), 5335–5356. Retrieved 2022-08-18, from http://doi.wiley.com/10.1029/1999JA900297 doi: 10.1029/1999JA900297

Kataoka, R., Shiota, D., Fujiwara, H., Jin, H., Tao, C., Shinagawa, H., & Miyoshi, Y. (2022). Unexpected space weather causing the reentry of 38 Starlink satellites in february 2022. *EartharXiv preprint*. Retrieved 2022-11-05, from https://eartharxiv.org/repository/object/3208/download/6447/ doi: 10.31223/X5GH0X

King, J. H., & Papitashvili, N. E. (2005). Solar wind spatial scales in and comparisons of hourly wind and ACE plasma and magnetic field data. *J. Geophys. Res.*, *110*, A02104. Retrieved from https://doi.org/10.1029/2004JA010649 doi: 10.1029/2004JA010649

Kivelson, M. G., & Hughes, W. J. (1990). On the threshold for triggering substorms. *Planetary and Space Science*, *38*(2), 211–220. Retrieved 2022-11-03, from https://linkinghub.elsevier.com/retrieve/pii/0032063390900855 doi: 10.1016/0032-0633(90)90085-5

Kokubun, S., McPherron, R. L., & Russell, C. T. (1977). Triggering of substorms by solar wind discontinuities. *Journal of Geophysical Research*, *82*(1), 74–86. Retrieved 2022-11-11, from http://doi.wiley.com/10.1029/JA082i001p00074 doi: 10.1029/JA082i001p00074

Koochak, Z., & Fraser-Smith, A. C. (2017). An update on the centered and eccentric geomagnetic dipoles and their poles for the years 1980–2015. *Earth and Space Science*, *4*(10), 626–636. Retrieved 2022-10-27, from https://onlinelibrary.wiley.com/doi/10.1002/2017EA000280 doi: 10.1002/2017EA000280

Kubyshkina, M., Tsyganenko, N., Semenov, V., Kubyshkina, D., Partamies, N., & Gordeev, E. (2015). Further evidence for the role of magnetotail current shape in substorm initiation. *Earth, Planets and Space*, *67*(1), 139. Retrieved 2022-11-03, from http://www.earth-planets-space.com/content/67/1/139 doi:

10.1186/s40623-015-0304-1

Laundal, K. M., Reistad, J. P., Hatch, S. M., Moretto, T., Ohma, A., Østgaard, N., ... Kloss, C. (2020). Time-scale dependence of solar wind-based regression models of ionospheric electrodynamics. *Scientific Reports*, *10*(1), 16406. Retrieved 2022-10-23, from https://www.nature.com/articles/s41598-020-73532-z doi: 10.1038/s41598-020-73532-z

Lee, D.-Y. (2004). Sawtooth oscillations directly driven by solar wind dynamic pressure enhancements. *Journal of Geophysical Research*, *109*(A4), A04202. Retrieved 2022-11-11, from http://doi.wiley.com/10.1029/2003JA010246 doi: 10.1029/2003JA010246

Li, H., Jiang, W., Wang, C., Verscharen, D., Zeng, C., Russell, C. T., ... Burch, J. L. (2020). Evolution of the Earth's magnetosheath turbulence: A Statistical study based on MMS observations. *The Astrophysical Journal*, *898*(2), L43. Retrieved 2022-11-18, from https://iopscience.iop.org/article/10.3847/2041-8213/aba531 doi: 10.3847/2041-8213/aba531

Liu, J., Wang, W., Zhang, B., Huang, C., & Lin, . (2018). Temporal variation of solar wind in controlling solar wind-magnetosphere-ionosphere energy budget. *Journal of Geophysical Research: Space Physics*, *123*(7), 5862–5869. Retrieved 2022-11-11, from https://onlinelibrary.wiley.com/doi/10.1029/2017JA025154 doi: 10.1029/2017JA025154

Lockwood, M. (1991). On flow reversal boundaries and transpolar voltage in average models of high-latitude convection. *Planetary and Space Science*, *39*(3), 397–409. Retrieved 2022-08-18, from https://linkinghub.elsevier.com/retrieve/pii/003206339190002R doi: 10.1016/0032-0633(91)90002-R

Lockwood, M. (2013). Reconstruction and prediction of variations in the open solar magnetic flux and interplanetary conditions. *Living Reviews in Solar Physics*, *10*, 4. Retrieved from https://doi.org/10.12942/lrsp-2013-4 doi: 10.12942/lrsp-2013-4

Lockwood, M. (2022). Solar wind—magnetosphere coupling functions: Pitfalls, limitations, and applications. *Space Weather*, *20*(2). Retrieved 2022-05-27, from https://onlinelibrary.wiley.com/doi/10.1029/2021SW002989 doi: 10.1029/2021SW002989

Lockwood, M., Bentley, S. N., Owens, M. J., Barnard, L. A., Scott, C. J., Watt, C. E., & Allanson, O. (2019). The development of a space slimatology: 1. Solar wind magnetosphere coupling as a function of timescale and the effect of data gaps. *Space Weather*, *17*(1), 133–156. Retrieved 2022-08-18, from https://onlinelibrary.wiley.com/doi/abs/10.1029/2018SW001856 doi: 10.1029/2018SW001856

Lockwood, M., Chambodut, A., Finch, I. D., Barnard, L. A., Owens, M. J., & Haines, C. (2019). Time-of-day/time-of-year response functions of planetary geomagnetic indices. *Journal of Space Weather and Space Climate*, *9*, A20. Retrieved 2022-08-18, from https://www.swsc-journal.org/10.1051/swsc/2019017 doi: 10.1051/swsc/2019017

Lockwood, M., & Cowley, S. W. H. (2022). Magnetosphere-ionosphere coupling: Implications of non-equilibrium conditions. *Frontiers in Astronomy and Space Sciences*, *9*, 908571. Retrieved 2022-08-18, from https://www.frontiersin.org/articles/10.3389/fspas.2022.908571/full doi: 10.3389/fspas.2022.908571

Lockwood, M., Cowley, S. W. H., & Freeman, M. P. (1990). The excitation of plasma convection in the high-latitude ionosphere. *Journal of Geophysical Research*, *95*(A6), 7961. Retrieved 2022-08-18, from http://doi.wiley.com/10.1029/JA095iA06p07961 doi: 10.1029/JA095iA06p07961

Lockwood, M., Haines, C., Barnard, L. A., Owens, M. J., Scott, C. J., Chambodut, A., & McWilliams, K. A. (2021). Semi-annual, annual and Universal Time variations in the magnetosphere and in geomagnetic activ-

ity: 4. Polar cap motions and origins of the Universal Time effect. *Journal of Space Weather and Space Climate*, *11*, 15. Retrieved 2022-08-18, from https://www.swsc-journal.org/10.1051/swsc/2020077 doi: 10.1051/swsc/2020077

Lockwood, M., Hairston, M., Finch, I. D., & Rouillard, A. P. (2009). Transpolar voltage and polar cap flux during the substorm cycle and steady convection events. *Journal of Geophysical Research: Space Physics*, *114*(A1), n/a–n/a. Retrieved 2022-08-18, from http://doi.wiley.com/10.1029/2008JA013697 doi: 10.1029/2008JA013697

Lockwood, M., & McWilliams, K. A. (2021a). On optimum solar wind-magnetosphere coupling functions for transpolar voltage and planetary geomagnetic activity. *Journal of Geophysical Research: Space Physics*, *126*(12). Retrieved 2022-05-28, from https://onlinelibrary.wiley.com/doi/10.1029/2021JA029946 doi: 10.1029/2021JA029946

Lockwood, M., & McWilliams, K. A. (2021b). A survey of 25 years' transpolar voltage data from the SuperDARN radar network and the expanding-contracting polar cap model. *Journal of Geophysical Research: Space Physics*, *126*(9). Retrieved 2022-08-18, from https://onlinelibrary.wiley.com/doi/10.1029/2021JA029554 doi: 10.1029/2021JA029554

Lockwood, M., McWilliams, K. A., Owens, M. J., Barnard, L. A., Watt, C. E., Scott, C. J., ... Coxon, J. C. (2020). Semi-annual, annual and Universal Time variations in the magnetosphere and in geomagnetic activity: 2. Response to solar wind power input and relationships with solar wind dynamic pressure and magnetospheric flux transport. *Journal of Space Weather and Space Climate*, *10*, 30. Retrieved 2022-08-18, from https://www.swsc-journal.org/10.1051/swsc/2020033 doi: 10.1051/swsc/2020033

Lockwood, M., & Morley, S. K. (2004). A numerical model of the ionospheric signatures of time-varying magnetic reconnection: 1. Ionospheric convection. *Annales Geophysicae*, *22*(1), 73–91. Retrieved 2022-08-18, from https://angeo.copernicus.org/articles/22/73/2004/ doi: 10.5194/angeo-22-73-2004

Lockwood, M., Owens, M. J., Barnard, L. A., Haines, C., Scott, C. J., McWilliams, K. A., & Coxon, J. C. (2020). Semi-annual, annual and Universal Time variations in the magnetosphere and in geomagnetic activity: 1. Geomagnetic data. *Journal of Space Weather and Space Climate*, *10*, 23. Retrieved 2022-08-18, from https://www.swsc-journal.org/10.1051/swsc/2020023 doi: 10.1051/swsc/2020023

Lockwood, M., Owens, M. J., Barnard, L. A., Scott, C. J., Frost, A. M., Yu, B., & Chi, Y. (2022). Application of historic datasets to understanding open solar flux and the 20th-century grand solar maximum. 1. Geomagnetic, ionospheric, and sunspot observations. *Frontiers in Astronomy and Space Sciences*, *9*, 960775. Retrieved 2022-09-01, from https://www.frontiersin.org/articles/10.3389/fspas.2022.960775/full doi: 10.3389/fspas.2022.960775

Lockwood, M., Owens, M. J., Barnard, L. A., Watt, C. E., Scott, C. J., Coxon, J. C., & McWilliams, K. A. (2020). Semi-annual, annual and Universal Time variations in the magnetosphere and in geomagnetic activity: 3. Modelling. *Journal of Space Weather and Space Climate*, *10*, 61. Retrieved 2022-08-18, from https://www.swsc-journal.org/10.1051/swsc/2020062 doi: 10.1051/swsc/2020062

Lockwood, M., Rouillard, A. P., Finch, I. D., & Stamper, R. (2006). Comment on "the *IDV* index: Its derivation and use in inferring long-term variations of the interplanetary magnetic field strength" by Leif Svalgaard and Edward W. Cliver. *Journal of Geophysical Research*, *111*(A9), A09109. Retrieved 2022-08-18, from http://doi.wiley.com/10.1029/2006JA011640 doi: 10.1029/2006JA011640

Longden, N., Chisham, G., Freeman, M. P., Abel, G. A., & Sotirelis, T. (2010). Estimating the location of the open-closed magnetic field line boundary from auroral images. *Annales Geophysicae*, *28*(9), 1659–1678. Retrieved 2022-11-01, from https://angeo.copernicus.org/articles/28/1659/2010/ doi: 10.5194/angeo-28-1659-2010

Lukianova, R. (2003). Magnetospheric response to sudden changes in solar wind dynamic pressure inferred from polar cap index. *Journal of Geophysical Research*, *108*(A12), 1428. Retrieved 2022-11-11, from http://doi.wiley.com/10.1029/2002JA009790 doi: 10.1029/2002JA009790

Lühr, H., Lockwood, M., Sandholt, P. E., Hansen, T. L., & Moretto, T. (1996). Multi-instrument ground-based observations of a travelling convection vortices event. *Annales Geophysicae*, *14*(2), 162–181. Retrieved 2022-08-18, from https://angeo.copernicus.org/articles/14/162/1996/ doi: 10.1007/s00585-996-0162-z

Mayaud, P.-N. (1972). The aa indices: A 100-year series characterizing the magnetic activity. *J. Geophys. Res.*, *77*(34), 6870–6874. Retrieved from https://doi.org/10.1029/ja077i034p06870 doi: 10.1029/ja077i034p06870

Milan, S. E., Boakes, P. D., & Hubert, B. (2008). Response of the expanding/contracting polar cap to weak and strong solar wind driving: Implications for substorm onset. *Journal of Geophysical Research: Space Physics*, *113*(A9), n/a–n/a. Retrieved 2022-10-23, from http://doi.wiley.com/10.1029/2008JA013340 doi: 10.1029/2008JA013340

Milan, S. E., Carter, J. A., Bower, G. E., Imber, S. M., Paxton, L. J., Anderson, B. J., ... Hubert, B. (2020). Dual-lobe reconnection and horse-collar auroras. *Journal of Geophysical Research: Space Physics*, *125*(10). Retrieved 2022-10-23, from https://onlinelibrary.wiley.com/doi/10.1029/2020JA028567 doi: 10.1029/2020JA028567

Milan, S. E., Carter, J. A., Korth, H., & Anderson, B. J. (2015). Principal component analysis of Birkeland currents determined by the Active Magnetosphere and Planetary Electrodynamics Response Experiment. *Journal of Geophysical Research: Space Physics*, *120*(12), 10,415–10,424. Retrieved 2022-11-12, from http://doi.wiley.com/10.1002/2015JA021680 doi: 10.1002/2015JA021680

Milan, S. E., Carter, J. A., Sangha, H., Bower, G. E., & Anderson, B. J. (2021). Magnetospheric flux throughput in the Dungey cycle: Identification of convection state during 2010. *Journal of Geophysical Research: Space Physics*, *126*(2), e2020JA028437. Retrieved from https://agupubs.onlinelibrary.wiley.com/doi/abs/10.1029/2020JA028437 doi: https://doi.org/10.1029/2020JA028437

Milan, S. E., Carter, J. A., Sangha, H., Laundal, K. M., Østgaard, N., Tenfjord, P., ... Anderson, B. J. (2018). Timescales of dayside and nightside field-aligned current response to changes in solar wind-magnetosphere coupling. *Journal of Geophysical Research: Space Physics*, *123*(9), 7307–7319. Retrieved 2022-11-12, from http://doi.wiley.com/10.1029/2018JA025645 doi: 10.1029/2018JA025645

Milan, S. E., Clausen, L. B. N., Coxon, J. C., Carter, J. A., Walach, M.-T., Laundal, K., ... Anderson, B. J. (2017). Overview of solar wind–magnetosphere–ionosphere–atmosphere coupling and the generation of magnetospheric currents. *Space Science Reviews*, *206*(1-4), 547–573. Retrieved 2022-10-23, from http://link.springer.com/10.1007/s11214-017-0333-0 doi: 10.1007/s11214-017-0333-0

Milan, S. E., Provan, G., & Hubert, B. (2007). Magnetic flux transport in the Dungey cycle: A survey of dayside and nightside reconnection rates. *Journal of Geophysical Research: Space Physics*, *112*(A1), n/a–n/a. Retrieved 2022-10-24, from http://doi.wiley.com/10.1029/2006JA011642 doi:

10.1029/2006JA011642

Mishin, V., & Karavaev, Y. (2017). Saturation of the magnetosphere during superstorms: New results from the magnetogram inversion technique. *Solar-Terrestrial Physics*, *3*(3), 28–36. Retrieved 2022-10-28, from http://naukaru.ru/en/nauka/article/18490/view doi: 10.12737/stp-33201704

Morley, S. K., & Lockwood, M. (2005). A numerical model of the ionospheric signatures of time-varying magnetic reconnection: 2. Measuring expansions in the ionospheric flow response. *Annales Geophysicae*, *23*(7), 2501–2510. Retrieved 2022-08-18, from https://angeo.copernicus.org/articles/23/2501/2005/ doi: 10.5194/angeo-23-2501-2005

Newell, P. T., & Gjerloev, J. W. (2011). Evaluation of SuperMAG auroral electrojet indices as indicators of substorms and auroral power. *Journal of Geophysical Research: Space Physics*, *116*(A12), 2011JA016779. Retrieved 2022-11-06, from https://onlinelibrary.wiley.com/doi/10.1029/2011JA016779 doi: 10.1029/2011JA016779

Newell, P. T., & Meng, C.-I. (1989). Dipole tilt angle effects on the latitude of the cusp and cleft/low-latitude boundary layer. *Journal of Geophysical Research: Space Physics*, *94*(A6), 6949–6953. Retrieved 2022-10-27, from http://doi.wiley.com/10.1029/JA094iA06p06949 doi: 10.1029/JA094iA06p06949

Owens, M. J., Lockwood, M., & Barnard, L. A. (2020). The value of CME arrival time forecasts for space weather mitigation. *Space Weather*, *18*(9). Retrieved 2022-08-18, from https://onlinelibrary.wiley.com/doi/10.1029/2020SW002507 doi: 10.1029/2020SW002507

Palmroth, M. (2004). Role of solar wind dynamic pressure in driving ionospheric Joule heating. *Journal of Geophysical Research*, *109*(A11), A11302. Retrieved 2022-11-11, from http://doi.wiley.com/10.1029/2004JA010529 doi: 10.1029/2004JA010529

Paxton, L. J., Morrison, D., Zhang, Y., Kil, H., Wolven, B., Ogorzalek, B. S., ... Meng, C.-I. (2002). Validation of remote sensing products produced by the Special Sensor Ultraviolet Scanning Imager (SSUSI): a far UV-imaging spectrograph on DMSP F-16. In A. M. Larar & M. G. Mlynczak (Eds.), (pp. 338–348). San Diego, CA. Retrieved 2022-11-01, from http://proceedings.spiedigitallibrary.org/proceeding.aspx?articleid=893287 doi: 10.1117/12.454268

Paxton, L. J., Zhang, Y., Kil, H., & Schaefer, R. K. (2021). Exploring the upper atmosphere: Using optical remote sensing. In W. Wang, Y. Zhang, & L. J. Paxton (Eds.), *Geophysical monograph series* (1st ed., pp. 487–522). Wiley. Retrieved 2022-11-01, from https://onlinelibrary.wiley.com/doi/10.1002/9781119815631.ch23 doi: 10.1002/9781119815631.ch23

Picone, J. M., Hedin, A. E., Drob, D. P., & Aikin, A. C. (2002). NRLMSISE-00 empirical model of the atmosphere: Statistical comparisons and scientific issues. *Journal of Geophysical Research: Space Physics*, *107*(A12), SIA 15–1–SIA 15–16. Retrieved 2022-11-05, from http://doi.wiley.com/10.1029/2002JA009430 doi: 10.1029/2002JA009430

Richmond, A. D., Ridley, E. C., & Roble, R. G. (1992). A thermosphere/ionosphere general circulation model with coupled electrodynamics. *Geophysical Research Letters*, *19*(6), 601–604. Retrieved 2022-11-06, from http://doi.wiley.com/10.1029/92GL00401 doi: 10.1029/92GL00401

Ridley, A. J., Gombosi, T. I., & DeZeeuw, D. L. (2004). Ionospheric control of the magnetosphere: conductance. *Annales Geophysicae*, *22*(2), 567–584. Retrieved 2022-11-10, from https://angeo.copernicus.org/articles/22/567/2004/ doi: 10.5194/angeo-22-567-2004

Robinson, R. M., & Zanetti, L. J. (2021). Auroral energy flux and joule heating derived from global maps of field-aligned currents. *Geophysical Research Letters*,

48(7). Retrieved 2022-11-01, from https://onlinelibrary.wiley.com/doi/10.1029/2020GL091527 doi: 10.1029/2020GL091527

Russell, C. T., & McPherron, R. L. (1973). Semiannual variation of geomagnetic activity. *Journal of Geophysical Research*, *78*(1), 92–108. Retrieved 2022-11-03, from http://doi.wiley.com/10.1029/JA078i001p00092 doi: 10.1029/JA078i001p00092

Sandhu, J. K., Rae, I. J., & Walach, M. (2021). Challenging the use of ring current indices during geomagnetic storms. *Journal of Geophysical Research: Space Physics*, *126*(2). Retrieved 2022-11-01, from https://onlinelibrary.wiley.com/doi/10.1029/2020JA028423 doi: 10.1029/2020JA028423

Schieldge, J., & Siscoe, G. (1970). A correlation of the occurrence of simultaneous sudden magnetospheric compressions and geomagnetic bay onsets with selected geophysical indices. *Journal of Atmospheric and Terrestrial Physics*, *32*(11), 1819–1830. Retrieved 2022-11-11, from https://linkinghub.elsevier.com/retrieve/pii/002191697090139X doi: 10.1016/0021-9169(70)90139-X

Shukhtina, M. A., Dmitrieva, N. P., Popova, N. G., Sergeev, V. A., Yahnin, A. G., & Despirak, I. V. (2005). Observational evidence of the loading-unloading substorm scheme. *Geophysical Research Letters*, *32*(17). Retrieved 2022-11-11, from http://doi.wiley.com/10.1029/2005GL023779 doi: 10.1029/2005GL023779

Siscoe, G. L. (1982). Polar cap size and potential: A predicted relationship. *Geophysical Research Letters*, *9*(6), 672–675. Retrieved 2022-10-23, from http://doi.wiley.com/10.1029/GL009i006p00672 doi: 10.1029/GL009i006p00672

Sivadas, N., & Sibeck, D. (2022). Regression bias in using solar wind measurements. *Frontiers in Astronomy and Space Sciences*, *9*, 924976. Retrieved 2022-07-07, from https://www.frontiersin.org/articles/10.3389/fspas.2022.924976/full doi: 10.3389/fspas.2022.924976

Smith, M. F., & Lockwood, M. (1996). Earth's magnetospheric cusps. *Reviews of Geophysics*, *34*(2), 233–260. Retrieved 2022-08-18, from http://doi.wiley.com/10.1029/96RG00893 doi: 10.1029/96RG00893

Southwood, D. J. (1987). The ionospheric signature of flux transfer events. *Journal of Geophysical Research*, *92*(A4), 3207. Retrieved 2022-11-11, from http://doi.wiley.com/10.1029/JA092iA04p03207 doi: 10.1029/JA092iA04p03207

Stauning, P., & Troshichev, O. A. (2008). Polar cap convection and PC index during sudden changes in solar wind dynamic pressure. *Journal of Geophysical Research: Space Physics*, *113*(A8), n/a–n/a. Retrieved 2022-11-11, from http://doi.wiley.com/10.1029/2007JA012783 doi: 10.1029/2007JA012783

Stubbs, T. J., R., V. R., Østgaard N., B., S. J., & A., F. L. (2005). Simultaneous observations of the auroral ovals in both hemispheres under varying conditions. *Geophysical Research Letters*, *32*(3), L03103. Retrieved 2022-10-27, from http://doi.wiley.com/10.1029/2004GL021199 doi: 10.1029/2004GL021199

Tanaka, T. (2007). Magnetosphere–ionosphere convection as a compound system. *Space Science Reviews*, *133*(1-4), 1–72. Retrieved 2022-11-10, from https://link.springer.com/10.1007/s11214-007-9168-4 doi: 10.1007/s11214-007-9168-4

Tsurutani, B. T., Green, J. L., & Hajra, R. (2022). The possible cause of the 40 SpaceX Starlink satellite losses in February 2022: Prompt penetrating electric fields and the dayside equatorial and midlatitude ionospheric convective uplift. *arXiv preprint*. Retrieved 2022-11-05, from https://arxiv.org/pdf/2210.07902 doi: 10.48550/arXiv.2210.07902

Tsyganenko, N. A. (2019). Secular drift of the auroral ovals: How fast do they actually move? *Geophysical Research Letters*, *46*(6), 3017–3023. Retrieved 2022-10-27, from https://onlinelibrary.wiley.com/doi/abs/10.1029/2019GL082159 doi: 10.1029/2019GL082159

Vorobjev, V. G., & Yagodkina, O. I. (2010). Seasonal and UT variations of the position of the auroral precipitation and polar cap boundaries. *Geomagnetism and Aeronomy*, *50*(5), 597–605. Retrieved 2022-10-27, from http://link.springer.com/10.1134/S0016793210050063 doi: 10.1134/S0016793210050063

Walach, M.-T., Milan, S. E., Yeoman, T. K., Hubert, B. A., & Hairston, M. R. (2017). Testing nowcasts of the ionospheric convection from the expanding and contracting polar cap model. *Space Weather*, *15*(4), 623–636. Retrieved 2022-10-25, from http://doi.wiley.com/10.1002/2017SW001615 doi: 10.1002/2017SW001615

Wang, X.-Y., Zhang, Q.-H., Wang, C., Zhang, Y.-L., Tang, B., Xing, Z.-Y., ... Wang, Y. (2022). An almost complete disappearance of open-flux polar cap for strongly northward interplanetary magnetic field. *Commun. Earth Environ.*, In Review. Retrieved 2022-10-23, from https://www.researchsquare.com/article/rs-1246727/v1 doi: 10.21203/rs.3.rs-1246727/v1

Weimer, D. R. (2005). Improved ionospheric electrodynamic models and application to calculating Joule heating rates. *Journal of Geophysical Research*, *110*(A5), A05306. Retrieved 2022-11-06, from http://doi.wiley.com/10.1029/2004JA010884 doi: 10.1029/2004JA010884

Wilson, G. R., Weimer, D. R., Wise, J. O., & Marcos, F. A. (2006). Response of the thermosphere to Joule heating and particle precipitation. *Journal of Geophysical Research*, *111*(A10), A10314. Retrieved 2022-11-06, from http://doi.wiley.com/10.1029/2005JA011274 doi: 10.1029/2005JA011274

Yamazaki, Y., & Maute, A. (2017). Sq and EEJ — a review on the daily variation of the geomagnetic field caused by ionospheric dynamo currents. *Space Science Reviews*, *206*(1-4), 299–405. Retrieved 2022-10-30, from http://link.springer.com/10.1007/s11214-016-0282-z doi: 10.1007/s11214-016-0282-z

Yue, C., Zong, Q. G., Zhang, H., Wang, Y. F., Yuan, C. J., Pu, Z. Y., ... Wang, C. R. (2010). Geomagnetic activity triggered by interplanetary shocks. *Journal of Geophysical Research: Space Physics*, *115*(A5), n/a–n/a. Retrieved 2022-11-11, from http://doi.wiley.com/10.1029/2010JA015356 doi: 10.1029/2010JA015356

Zhang, X., Wang, C., Chen, T., Wang, Y. L., Tan, A., Wu, T. S., ... Wang, W. (2005). Global patterns of Joule heating in the high-latitude ionosphere. *Journal of Geophysical Research*, *110*(A12), A12208. Retrieved 2022-11-20, from http://doi.wiley.com/10.1029/2005JA011222 doi: 10.1029/2005JA011222

Zhang, Y., Paxton, L. J., Schaefer, R., & Swartz, W. H. (2022). Thermospheric conditions associated with the loss of 40 Starlink satellites. *Space Weather*, *20*(10). Retrieved 2022-10-29, from https://onlinelibrary.wiley.com/doi/10.1029/2022SW003168 doi: 10.1029/2022SW003168

Øye, S. (2018). *Parametrization of the nightside reconnection rate during times with contracting polar caps* (Master's thesis, Department of Physics, University of Oslo, Norway). Retrieved 2022-11-03, from https://www.duo.uio.no/bitstream/handle/10852/64071/8/Master.pdf

8 Open Research

The data used in this study are all openly available. The interplanetary data are available from the Physics Data Facility (SPDF) at NASA's Goddard Space Flight Center as the Omni composite from https://omniweb.gsfc.nasa.gov/ow_min.html. The am indices are available from the International Service of Geomagnetic Indices (ISGI) at http://isgi.unistra.fr/data_download.php. The SuperMAG SML and SMR indices are available from the SuperMAG project website at the Johns Hopkins Univer-

sity Applied Physics Laboratory at `http://supermag.jhuapl.edu/indices/`. The SYM-H index is available from the World Data Center for Geomagnetism,Kyoto at `http://wdc.kugi.kyoto-u.ac.jp/`. The Kp geomagnetic index is available from Geomagnetic Observatory Niemegk, GFZ German Research Centre for Geosciences at `https://www-app3.gfz-potsdam.de/kp_index/Kp_ap_since_1932.txt` The DMSP SSUSI images are available from the SSUSI project website at the Johns Hopkins University Applied Physics Laboratory `http://ssusi.jhuapl.edu/`.

Acknowledgments

The authors are grateful to the many instrument scientists and engineers who make the datasets employed in this study possible and the staff of a number of datacentres who allow easy access to the data. These include: the Space Physics Data Facility (SPDF) at NASA's Goddard Space Flight Center for the Omni composite of interplanetary observations; the International Service of Geomagnetic Indices (ISGI), France and collaborating institutes for the am geomagnetic indices; the World Data Center for Geomagnetism, Kyoto for the SYM-H index; the PIs and staff of the many groups contributing data to the SuperMAG project, coordinated at The Johns Hopkins University Applied Physics Laboratory, for the SMR and SML indices; The Geomagnetic Observatory Niemegk, GFZ German Research Centre for Geosciences for the Kp index; The Air Force Defense Meteorological Satellite Program (DMSP) and, in particular, the Special Sensor Ultraviolet Spectrographic Imagers (SSUSI) project at The Johns Hopkins University Applied Physics Laboratory. This work is supported by a number of grants: consolidated grants number ST/R000921/1 and ST/V000497/1 from the United Kingdom Science and Technology Facilities Council (UKRI/STFC) and the SWIGS Directed Highlight Topic Grant number NE/P016928/1/ and grant NE/S010033/1 from the United Kingdom Natural Environment Research Council (UKRI/NERC). The authors are also grateful to Steve Milan for valuable discussions of this work.